공학박사 학위논문

Nanophotonic Elements for High-Resolution CMOS Image Sensors

고해상도 CMOS 이미지 센서를 위한 나노광학소자

2021년 8월

서울대학교 대학원

전기·정보공학부

홍 종 우

Nanophotonic Elements for High-Resolution CMOS Image Sensors

지도 교수 이 병 호

이 논문을 공학박사 학위논문으로 제출함
2021년 8월

서울대학교 대학원
전기 · 정보공학부
홍 종 우

홍종우의 공학박사 학위논문을 인준함
2021년 8월

위 원 장 ______________________

부위원장 ______________________

위 원 ______________________

위 원 ______________________

위 원 ______________________

Abstract

Nanophotonic elements for high-resolution CMOS image sensors

Jongwoo Hong

Department of Electrical Engineering and Computer Science

College of Engineering

Seoul National University

Image sensor is a device that converts electromagnetic waves scattered by the objects or environment into electric signals. Recently, in the mobile device and autonomous vehicle industries, multiple image sensors having different purposes are required for a single device. In particular, image sensors with more than 100 million pixels are being developed in response to the development of a display to a high resolution of 8K or more. However, due to the limited space of the mobile device, the size of pixels constituting the sensor must be reduced for a high-resolution image sensor, which causes factors that reduce image quality, such as a decrease in light efficiency, a decrease in quantum efficiency, and color interference.

Metasurface is a device that modulates electromagnetic waves through an array of antennas smaller than wavelength. It has been proposed as a device that replaces the color filter, lens, and photodiode constituting the optical system of the image sensor. However, the performance of the metasurface corresponding to the miniaturized pixel size was limited by the operating principle that requires several array of nano-antennas. In this dissertation, I present a metasurface optical device that can improve the image quality of an existing image sensor composed of micropixels.

First, an absorption type color filter that suppresses reflection is discussed. The reflection that inevitably occurs in the conventional metasurface color filter elements causes a flare phenomenon in the captured image. In this dissertation, I design a color filter that transmits only a specific band and absorbs the rest of the absorption resonant band of a hyperbolic metamaterial antenna using a particle swarm optimization method. In particular, I present a Bayer pattern color filter with a pixel size of 255 nm.

Second, I introduce a color distribution meta-surface to increase the light efficiency of the image sensor. Since the photodiode converts light having energy above the band gap into an electric signal, an absorption type color filter is used for color classification in image sensor. This means that the total light efficiency of the image sensor is limited to 33% by the blue, green, and red filters constituting one pixel. Accordingly, a freeform metasurface device is designed that exceeds the conventional optical efficiency limit by distributing light incident on the sub-pixel in different directions according to color.

Finally, an optical confinement device capable of increasing signal-to-noise ratio (SNR) in low-illuminance at near-infrared is presented. Through the funnel-shaped plasmonic aperture, the light is focused on a volume much smaller than the wavelength. The focused electric and magnetic fields interact with the spatially distributed semiconductors, which achieve a Purcell effect enhanced by the presence of the metasurface.

This dissertation is expected to overcome the conventional nanophotonic devices for image sensors and become a cornerstone of the development of micropixel or nanopixel image sensors. Furthermore, it is expected to contribute to building a new image sensor platform that will replace the optical system constituting the image sensor with metasurface.

Keywords: CMOS image sensor, metasurface, color filter, color splitter, hyperbolic metamaterial, surface plasmon polariton
Student Number: 2015-21010

Contents

Abstract i

Contents iv

List of Tables vi

List of Figures vii

Chapter 1 Introduction 1

1.1 Overview of CMOS image sensors 1

1.2 Toward high-resolution miniaturized pixel 2

1.3 Nanophotonic elements for high-resolution camera 3

1.4 Dissertation overview 5

Chapter 2 Light interaction with subwavelength antennas 7

2.1 Overview of plasmonic antenna 7

2.2 Overview of dielectric metasurface 9

2.3 Overview of hyperbolic metamaterials 11

Chapter 3. Absorptive metasurface color filter based on hyperbolic metamaterial for noise reduction 14

3.1 Introduction 14

3.2 Principle of hyperbolic metamaterial absorbers 17

3.3 Absorptive color filter design based on particle swarm optimization method 19

3.4 Numerical analysis on optimized metasurface color filters 23

3.4.1 Single color filter optimization 23

3.4.2 Angle tolerance for optimized metasurface color filters 26

3.5 Sub-micron metasurface color filter array 29

3.6 Conclusion 35

Chapter 4 High-efficient full-color pixel array based on freeform nanostructures for high-resolution image sensor 37

4.1 Introduction 37

4.2 Optimization of metasurface full-color splitter 40

4.3 Implementation of color splitters 46
4.4 Image quality evaluation... 52
4.5 Discussion about off-axis color splitters.. 55
4.6 Conclusion 59
Chapter 5 Plasmonic metasurface cavity for simultaneous enhancement of optical electric and magnetic fields 60
5.1 Introduction.. 60
5.2 Working principle and numerical results 63
5.2.1 Principle of funnel-shaped metasurface cavity 63
5.2.2 Discussion 67
5.3 Experimental results 69
5.4 Purcell effect.. 72
5.5 Conclusion 74
Chapter 6 Conclusion... 75
Appendix 78
A.1 Colorimetry.. 78
A.2 Color difference CIEDE2000... 79
B. Related work 80
Bibliography 82

List of Tables

Table 1.1 Main subjects of each chapter in terms of functions about color filter, color splitter, and quantum efficiency. 6
Table 3.1. Optimized geometry parameters for MCF..................................... 24
Table 3.2. Optimized geometry parameters for metasurface color filter array 29

List of Figures

Figure 2.1 (a) A schematic of surface plasmon and (b) its dispersion relation . 7
Figure 2.2 A schematic of radiation pattern from (a) hole and (b) particle 9
Figure 2.3 Interaction between light and subwavelength antenna arrays shaped by (a) rectangular and (b) circular symmetric nano-structure 10
Figure 2.4 Examples of hyperbolic metamaterials constructed by alternative vertical stacks and nanowire array of metal-dielectric 12
Figure 2.5 (a) Effective permittivity of alternatively vertical stack of Al-SiO_2. (b) Isofrequency curves of Al-SiO2 stack in visible wavelength range. 13
Figure 3.1 Examples of subwavelength unit-cells that have been employed depending on functions. (a) Rods (i, iii) and apertures (ii, iv) composed of dielectric (i, ii) and metal (ii, iv) for narrow band scattering. (b) Metal-dielectric-metal structure for narrowband absorption. (c) Spatial multiplexing of multiple rods for broadband coupling. 15
Figure 3.2 (a) Schematic diagram of effective cylindrical HMM waveguide. (b) Effective refractive index along reduced radius (k_0a) calculated by characteristic equation at 400 nm (blue), 550 nm (green), and 700 nm (red). (c) Power flow along propagation axis. Solid lines (light purple box) and dashed lines (light yellow box) denote forward and backward modes, respectively. (d) Absorption spectrum for wavelength and radius.. 18
Figure 3.3 Proposed metasurface and optimization process. (a) Unit-cell diagram composed of alternative Al-SiO_2 layers with 100 nm-thick silica spacer on silicon substrate and variable filling ratio. Light is normally incident with polarization-independency. (b) Scattering

process in proposed MCF consisting of metasurface (layer 1), SiO_2 spacer (layer 2), and Si substrate (layer 3). (c) Intensity of multiple reflection inside spacer for RGB color filters. 20
Figure 3.4. Optimization process. (a) Unit-cell diagram composed of 12 Al-SiO_2 layers with variable filling ratio in FDTD simulation. (b) Gaussian lineshape for target center wavelengths of 460, 530, and 650 nm with 50 % efficiency. (c) A schematic of particle swarm optimization. Particle, M-dimensional coordinate, and particle position correspond to FDTD simulation, parameter space, and optimized parameters, respectively. 21
Figure 3.5 Transmission and reflection spectra from optimized metasurface for (a) blue, (b) green, and (c) red color. Insets in (a–c) depict perceptual colors from CIELAB. Dashed lines at 460 nm, 530 nm, and 650 nm indicate center wavelengths of target spectrum. (d)–(f) *XZ* cross-sections of enlarged optimized meta-atoms and normalized electric field at target wavelengths. White dotted lines denote boundary of meta-atom and substrate. White arrows indicate the spatial position of electric field resonances excited by meta-atom and transmitted light. 24
Figure 3.6 Colors calculated from CIELAB space. Transmission and reflection spectra correspond to each point and color on (a) L^*a^* and L^*b^* coordinates, and (b) a^*b^* coordinate. The points in gray ellipse represent reflection colors. (c) Transmission and reflection ratio. 26
Figure 3.7 Incident angle dependence in terms of polarization of (a-c) TE modes and (d-f) TM modes. (a, d) Schematic diagrams of TE and TM incidence. (b, e) Chromaticity variation in a^*b^* coordinates. The dots are distributed in increase of 5 degrees along black arrows. (c, f) Color difference expressed by CIEDE2000 from

CIELAB with respect to incident angle. The light gray boxes denote just-noticeable region. 28
Figure 3.8 (a) Schematic diagram of MCFA and material distribution at the cross-section of each meta-atom. (b) Transmission and reflection spectra from optimized MCFA for entire RGB pixel. (c) Color distribution on CIELAB space. 30
Figure 3.9 (a) Transmission-reflection ratio about Bayer pattern MCFA. (b) The SNRs among colors in each color pixels............................... 31
Figure 3.10 Color simulation from Gretag-Macbeth color chart for single MCFs and Bayer MCFA. The white dashed squares denote calculated color by the proposed MCFA and conventional dye color filters. 32
Figure 3.11 (a) Fabrication process. The SiO_2 spacer is deposited and Al-SiO_2 layers are alternatively deposited. And then FIB milling is performed by Ga^+ ion. (b) Color tolerance by geometric fabrication error for randomly distributed error from -10 to 10 nm of individual layer-thickness and bottom/top diameters. (c) Examples of color tolerance from -20 to 20 nm of bottom/top diameters simultaneously and from -10 nm to 10 nm of all layer thickness. (d) Cross-sections of rounded-tip structure with its transmission and reflection spectra where solid-lines and dashed-lines denote spectra of optimized color filter and with rounding errors. 35
Figure 4.1 (a) A schematic of freeform metasurface full-color splitter for sub-pixel (b) Integration scheme of sub-pixel color splitters. 39
Figure 4.2 Summarized flow chart of optimization process based on gradient of refractive index distribution 40
Figure 4.3 (a-c) Optimized freeform metasurface cross-section of RBG, BGR, and GRB in order of (1^{st}, 0^{th}, -1^{st}), respectively. Purple area means SiN distribution. (d-f) Corresponding diffraction efficiencies. Each

colored area surrounded by two line-graphs from x- and y-polarized illumination denotes polarization tolerance. (g-f) Color distribution on CIELAB coordinates with respect to L^*, a^*, and b^*.43
Figure 4.4 Color distribution on CIE 1931 analyzed by diffraction efficiency of (a) RBG, (b) BGR, and (c) GRB metasurfaces. 44
Figure 4.5 (a) Effective refractive indices of eigenmodes in freeform metasurface layer for RBG color splitter at λ = 680 nm. (b-f) Magnetic intensity $|\mathbf{H}|^2$ distributions of propagation modes. 45
Figure 4.6 Fabrication process of the proposed metasurface that follows traditional e-beam lithography process with ICP RIE. 46
Figure 4.7 Process of GDS file generation for desired freeform pattern. (a) Detected edge of the optimized BGR pattern and (b) its enlarged pattern. (c) Convert zigzag polylines into a single line. (d) Vertices of polylines after (c) and (e) its reduced vertices. (f) Exposure patterns in E-beam lithography from (d) and (g) patterns from (e).46
Figure 4.8 (a) Schematic diagram of experimental set-up. (b) Fabricated sample image captured by FE-SEM with 1 μm of scale bar. (c) Experimental results at Fourier plane at three wavelengths. Each column of (b-d) corresponds to an individual color splitter. 49
Figure 4.9 (a) Schematic illustration of the designed color splitter array in order of RBG, GRB, and BGR along x-direction. (b) Optical efficiency at the distance of d = 2.33 μm from color splitter. (c) Normal-directional Poynting vector. (d) Color crosstalk in each sub-pixel. 50
Figure 4.10 (a) FE-SEM image of integrated color splitters. The white scale bar denotes 3 μm. (b) Measured image at the distance of 2.33 μm from metasurface. 52
Figure 4.11 (a) Macbeth color checker to calibrate color as reference color. (b)

Color checker passing through the proposed metasurface. (c) Color checker calibrating through color correction matrix. (d) Color checker passing through the conventional dye color filters. (e) Color difference 2000 between (a) and (b). (f) Color difference between (a) and (c). 53

Figure 4.12 (a) Image PSNR under the additive Gaussian noise defining sensor PSNR to raw image for the conventional color filter, the proposed metasurface, and the metasurface with color correction matrix. The reference image is full color "OEQE" letters. (b) Raw image and its PSNR for 10, 20, and 30 dB of sensor PSNR. 54

Figure 4.13 Coordinate for oblique incidence on metasurface........ 55

Figure 4.14 Optimized patterns of GRB color splitter and its diffraction efficiencies for $\theta=\left[-10^{\circ},-20^{\circ}\right]$ and $\phi=\left[0^{\circ},15^{\circ},30^{\circ}\right]$. 56

Figure 4.15 Optimized patterns of RBG color splitter and its diffraction efficiencies for $\theta=\left[-10^{\circ},-20^{\circ}\right]$ and $\phi=\left[0^{\circ},15^{\circ},30^{\circ}\right]$. 57

Figure 4.16 Optimized patterns of BGR color splitter and its diffraction efficiencies for $\theta=\left[-10^{\circ},-20^{\circ}\right]$ and $\phi=\left[0^{\circ},15^{\circ},30^{\circ}\right]$. 58

Figure 5.1 (a) A schematic of the proposed metasurface. (b) Transverse field distribution of current, electric and magnetic field. 64

Figure 5.2 Plasmonic field distribution at the interface between (a) gold/glass and (b) air/gold with SP wavelength. (c) Radiation pattern of *z*-directional electric field along circle of 1.5 μm radius. 66

Figure 5.3 (a) Average electromagnetic intensity enhancement in NC region. (b) Electric and magnetic energy density distribution at the middle of metal film. 67

Figure 5.4 Scattering cross-section from decomposed multipoles........ 69

Figure 5.5 (a) Fabrication process of the proposed metasurface (b) SEM image of fabricated metasurface.. 70

Figure 5.6 (a) Schematic illustration of the custom-built spectroscopy. (b) Normalized transmission spectra by FEM calculation and experimental measurement.. 72

Figure 5.7 (a) Schematic illustration of the custom-built NSOM. (b) Measured electric field and simulation result on the surface on metasurface.72

Figure 5.8 Radiative and non-radiative decay rates calculated by dipole source. The solid lines and dashed lines denote radiative and non-radiative decay rate, respectively. 74

Figure A.1 (a) Tristimulus values of the CIE 1931 standard colorimetric observer. (b) Relative power spectrum of standard illuminant D65.79

Chapter 1 Introduction

1.1 Overview of CMOS image sensors

A complementary metal oxide semiconductor (CMOS) image sensor, which converts optical signals into electrical ones, is an optical system that relays light from environment to handy camera sensor without degradation [1]. Scattered light interacted with environment is transferred to CMOS image sensor (CIS) through camera lenses, sampled by pixels, and then converted to electric currents in photodiodes. After electronically processing the pixelated current distribution, digitalized image is recorded. In this whole process from scattered light to digital image, optical elements result in image quality that contains brightness, sharpness, contrast, dynamic range, color accuracy, resolution, quantum efficiency, and signal-to-noise ratio (SNR) [2]. Thus, it is important to understand correlation between optical elements and those factors affecting image quality.

The camera lenses manipulate brightness by iris, color accuracy from aberration correction, and modulation transfer function (MTF) that characterizes contrast and sharpness [3]. Meanwhile, in optical system of modern CIS, typical pixels consist of micro-lens, bandpass filter, and photodiode. The micro-lens pixelates the transferred light from camera lens into high quantum efficiency and signal-to-noise ratio [4]. Before reaching the photodiode, the light is collected in suitable wavelength band by color filters, IR filter, or etc. according to the purpose. The photodiode absorbs photon that has energy higher than band gap of material and generates electron-hole pair of which ratio denotes quantum efficiency [5].

1.2 Toward high-resolution miniaturized pixel

Following development of high-resolution display from large-area to near-eye display, high resolution cameras are on demand for videos or pictures [6]. The resolution is simply defined by the ratio of sensor size and pixel size, so that high-resolution can be achieved by reducing pixel size and enlarging sensor size. For mobile phone, modern CIS requires much smaller sensor size than one of full-frame digital single-lens reflex or mirror-less cameras due to physical size of device. For example, 0.64 μm pixel size of Samsung ISOCELL 2.0 as 50 mega-pixels is about 5.84 times smaller than one of Sony A7R4 as 60 mega-pixels in full-frame CIS. For high-resolution sensor, the pixel size in mobile CIS needs to be smaller. This implies that each pixel accommodates comparable photons with noise, which makes difficult to capture good-quality photo under low light condition, especially [7]. Moreover, miniaturized pixels have been suffered from electrical and optical crosstalk among neighboring pixels.

In this regard, advanced image sensor technologies have allowed pixel size to shrink into 0.64 μm, which includes backside-illumination (BSI) structure to reduce optical loss by circuit loss, isolation layer to minimize neighboring crosstalk, vertical channel transfer gate to boost full-well capacity (FWC) that relates to dynamic range, and more pixel binning [8-12].

1.3 Nanophotonic elements for high-resolution camera

Metasurface optical elements that consist of subwavelength antenna array have given insight into replacement of conventional bulk optical elements for ultra-compact form factor device thanks to their high degree of freedom and subwavelength operation [13]. The metasurface have been demonstrated for lens, hologram, polarizer, and color applications by modulating amplitude or phase of light [14-17]. Especially, the metasurfaces suggest insight into replacement of optical elements in image sensors such as lenses, color filters, and photodiodes. As a part of color filter, a cluster of subwavelength antennas filters light spectrum by utilizing dielectric resonance and transmits target wavelength by plasmonic resonance [18]. To deal with efficiency limitation of conventional color filter array, wavelength-dependent light guiding has been reported, which is based on spatial multiplexed metalens, multi-layer freeform metagrating, and pixel-scale color splitters [19-22]. In regard to quantum efficiency of photodiode, light trapping in subwavelength volume has been investigated [23, 24]. In this dissertation, issues from metasurface optical elements for image sensor are concerned including color filter, color splitter, and field confinement as below.

The first deliberation is noise of conventional metasurface color filter. The conventional organic color filters comprised of pigment or dye absorb unwanted wavelengths and pass through wanted wavelengths. In contrast with their absorptive property, most of metasurface color filters manipulate resonant reflection for dielectric metasurface and resonant transmission for plasmonic metasurface [18]. This indispensable reflection from previous metasurface color filters always exists that might lower image quality, giving rise to flare effect or ghost image by multiple reflection in CIS. Thus, absorption-based metasurface color filters with suppressed reflection is indisputably required that operates like conventional pigment or dye color filters [25].

The second issue is related to transmission efficiency of color filter. As abovementioned, the conventional color filters are unavoidable to limit transmission efficiency because of the use of absorptive materials. To circumvent this loss, previous studies that substitute for color filter divide the light into red, green, and blue (RGB) sub-pixels suppressing absorption. For example, spatially multiplexed metalenses that can disperse wavelength-dependent focal points have been reported [19]. In addition to metalens, micrometer color splitters have been realized by using diffractive element such as rectangular nanorods and three-dimensional freeform voxel [26, 27]. In the case of metalens-based devices, they need several times as large area as wavelength, which is not suitable for sub-micron pixel. Furthermore, the diffractive color splitters using nanorods were suffered from color purity by direct white light incidence channel [21, 28]. Even though Camayd-Muñoz *et al*. suggested color voxels, it could not be realized due to its structure complexity [27]. Thus, single-layered color splitter without white channel could be worthy.

The third application that related with photodiode is field confinement in subwavelength volume. The incident light is distributed by pixel-by-pixel and absorbed by photodiode layer that composed of silicon (Si) for visible wavelength or indium gallium arsenide (InGaAs) for near infrared wavelength. To enhance absorption in miniaturized modern CIS, thickness of photodiodes needs to be several times as long as wavelength [11]. Thus, the field confinement in subwavelength volume could be meaningful which compress the photodiode in subwavelength thickness. This issue is handled by plasmonic cavity array by aperture shape manipulation [29].

1.4 Dissertation overview

This dissertation describes metasurface optical elements for miniaturized CIS. The object of this dissertation focuses on improvement of conventional metasurface optical elements that might replace optical elements of modern CIS, which is summarized in Table 1.1. From scratch, principles of plasmonic, dielectric, and hybrid metasurface are illustrated in Chapter 2, which are based on field confinement, color splitter, and color filter applications in the dissertation.

Chapter 3 introduces absorptive type color filters that reduce reflection with very short pixel pitch. To avoid reflection from dielectric or metal, dielectric-metal composite absorber is adopted for building blocks. The antenna design is based on particle swarm optimization method. In addition, color analysis is applied to establish device performance.

Chapter 4 aims to break through transmission efficiency of conventional color filters that have the maximum of 33 % for RGB pixel. Gradient-based inverse design of freeform metasurface is utilized for color splitters. Unlike absorptive color filters, incident colors are guided into neighboring pixel to additive efficiency.

Chapter 5 represents plasmonic field enhancement metasurface that amplifies light-matter interaction. This function can be attributed to photon-electron conversion efficiency and increased SNR.

Finally, Chapter 6 summarizes this dissertation and presents the feasibility of metasurface for future miniaturized CIS.

Table 1.1 Main subjects of each chapter in terms of functions about color filter, color splitter, and quantum efficiency.

Image sensor	Chapter	Goal	Function	Proposed metasurface
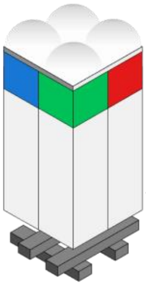	2	Noise reduction	Color filter	▪ Hyperbolic tapered 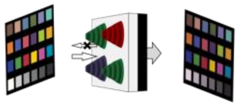
	3	Optical efficiency	Color splitter	▪ Dielectric freeform 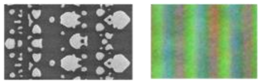
	4	Quantum efficiency	Field enhancement	▪ Plasmonic funnel 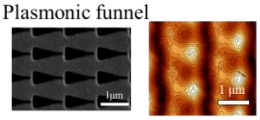

Chapter 2 Light interaction with subwavelength antennas

Throughout this dissertation, materials consisting of metasurface are metals and dielectrics. Light interaction with metal and dielectric shows different ways due to existence of free electrons in conductor. For metallic material, light induces collectively oscillating electrons at metal-dielectric interface. On the other hand, light coupling with dielectric have been utilized for high efficient device due to less absorptive scattering than metal. This chapter briefly reviews characteristics of meta-atoms in perspective of composed materials.

2.1 Overview of plasmonic antenna

Surface plasmon polaritons (SPPs) are bounded mode at metal-dielectric interface, which propagates along the metal-dielectric interface but evanescently decay along vertical direction to interface. The SPP is induced by Maxwell equation and metal-dielectric interface as shown in Figure 2.1(a).

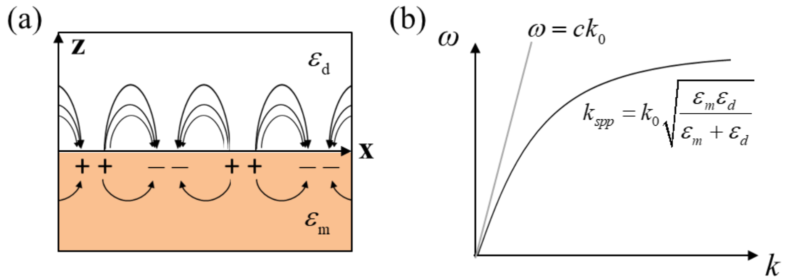

Figure 2.1 (a) A schematic of surface plasmon and (b) its dispersion relation

For transverse magnetic (TM) modes in normal incidence, electric field and magnetic fields are represented as

$$\left[E_x, H_y, E_z\right] = \begin{cases} H_0\left[-\dfrac{jk_d}{\omega\varepsilon_0\varepsilon_d}, 1, -\dfrac{k_{spp}}{\omega\varepsilon_0\varepsilon_d}\right]e^{jk_{spp}x}e^{-k_d z},\ z > 0, \\ H_0\left[-\dfrac{jk_d}{\omega\varepsilon_0\varepsilon_m}, 1, -\dfrac{k_{spp}}{\omega\varepsilon_0\varepsilon_m}\right]e^{jk_{spp}x}e^{k_m z},\ z < 0, \end{cases} \tag{2.1}$$

where $k_{(d,\,m)}$ is $n_{(d,\,m)}k_0$, and the propagation vector of SPP is

$$k_{\mathrm{spp}} = k_0\sqrt{\frac{\varepsilon_m\varepsilon_d}{\varepsilon_m + \varepsilon_d}},$$

where m and d denote metal and dielectric. Since the propagation vector of SPP has smaller than one of free space wave, the SPP can be used for light manipulation in subwavelength scale [30]. However, to excite SPP from free space light with momentum k_0, it needs to be matched with momentum k_{spp} by using prism or gratings.

One of notable phenomena in SPP is extraordinary optical transmission (EOT) where the light can pass through subwavelength hole on metal film [31]. When the light illuminates on subwavelength hole, free electrons at edge of hole oscillate resonantly like dipole source as shown in Figure 2.2(a). This oscillation induces SPP mode that propagates through metal-dielectric-metal hole. On opposite side, propagating SPPs are scattered like dipole radiation in near-field and far-field. From this, the shape and distribution of hole enable to manipulate near-field distribution, and tailor far-field modulation [32, 33].

Furthermore, subwavelength rods or particles that are the complementary structure of hole in Figure 2.2(b) function similar way to holes that support localized surface plasmon resonance (LSPR) depending on particle size. Light incidence on particle brings charge oscillation in multipolar distribution with near-field enhancement and the light is scattered with interference of multipolar radiation.

Thus, the plasmonic metasurfaces that is congregation of subwavelength plasmonic antennas have been applied to near-field focusing, photo-luminescence enhancement, and far-field manipulation by designing shape and distribution of holes or particles.

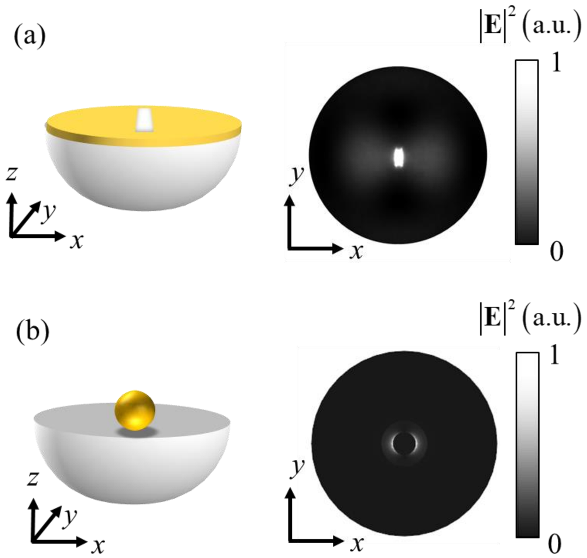

Figure 2.2 A schematic of radiation pattern from (a) hole and (b) particle

2.2 Overview of dielectric metasurface

Dielectric metasurfaces have attracted much attention thanks to its high efficiency rather than attenuation by lossy metal. Compared to plasmonic metasurface, most of antennas consisting of dielectric metasurface operate as combination of effective waveguide modes [34]. To understand light modulation by subwavelength antenna, rectangular and circular antenna is given in Figure 2.3. When incident light is coupled with rectangular antenna, the light propagates along sum of effective modes. By the anisotropic shape of rectangular antenna, total field can be considered as decomposition of orthogonal modes along long and short axes. Each mode is guided with effective mode indices $n_{\mathrm{eff},1}$ and $n_{\mathrm{eff},2}$. And then, interference of scattered light at far-field determines light modulation that includes amplitude, phase, and polarization state. Circular polarized light, which is combination of orthogonal linear polarization states with pi/2 phase difference, is modulated by different propagation phase hk_{eff}, where h and $\underline{k}_{\mathrm{eff}}$ denote height of antenna and effective propagation vector. This results in geometric phase or Phancharatnam-Berry phase as shown in Figure 2.3(a). In addition, when the light is incident on circular shaped antenna, the light is identically modulated for arbitrary polarization state due to circular symmetry of antenna [35]. In general, arbitrary antenna shape can give rise to anomalous effects due to coupling among effective modes, such as Fano resonance and Kerker effects [36, 37].

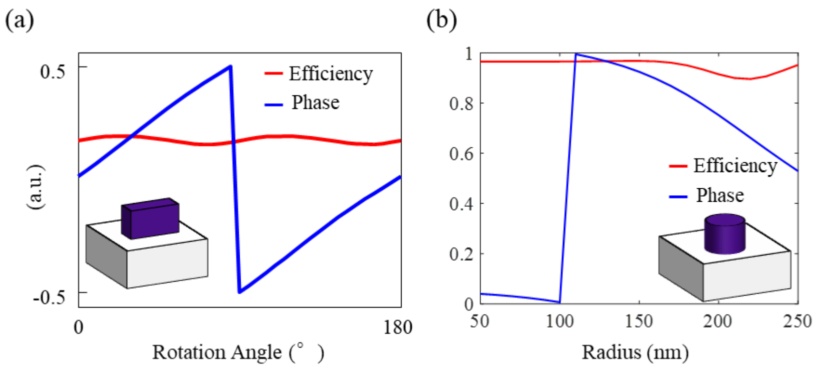

Figure 2.3 Interaction between light and subwavelength antenna arrays shaped by (a) rectangular and (b) circular symmetric nano-structure

2.3 Overview of hyperbolic metamaterials

Materials composed of metasurface could be hybrid materials that synthesize dielectric and metal. If individual material accounting for single antenna is distributed in the size of deep-subwavelength, light regards the composite material composed of antenna as single effective material [38, 39]. The macroscopic optical properties of effective material can be described by effective medium approximation, which is defined by volume fraction of materials and structure consisting of effective media. In the case of periodic array along *z*-direction and uniform distribution along *xy*-direction as shown in the left diagram of Figure 2.4, effective electric permittivity is given by anisotropic electric permittivity tensor,

$$\overleftrightarrow{\varepsilon} = \begin{bmatrix} \varepsilon_p & 0 & 0 \\ 0 & \varepsilon_p & 0 \\ 0 & 0 & \varepsilon_v \end{bmatrix} \tag{2.2}$$

and

$$\begin{aligned} \varepsilon_p &= f\varepsilon_m + (1-f)\varepsilon_d \\ \varepsilon_v &= \left(\frac{f}{\varepsilon_m} + \frac{1-f}{\varepsilon_d}\right)^{-1}, \end{aligned} \tag{2.3}$$

where f, ε_p, ε_v, ε_d, and ε_m denote metal ratio, electric permittivity of parallel direction, vertical direction, dielectric and metal, respectively.

For example, the vertical stack of 50:50 of aluminum (Al) and silicon dioxide (SiO_2) of which optical constant is obtained from Refs [40] and [41], the electric permittivity along parallel axis is negative while one along vertical axis is positive in visible range as shown in Figure 2.5(a). This opposite sign of electric permittivity results in hyperbolic shaped isofrequency curves described by Eq. (2.4), which is called hyperbolic metamaterials (HMMs).

$$\frac{k_p^2}{\mathrm{Re}(\varepsilon_v)}+\frac{k_v^2}{\mathrm{Re}(\varepsilon_p)}=k_0^2 \tag{2.4}$$

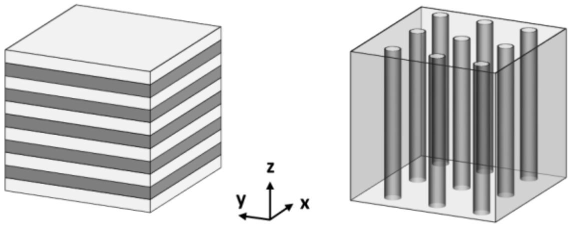

Figure 2.4 Examples of hyperbolic metamaterials constructed by alternative vertical stacks and nanowire array of metal-dielectric

The hyperbolic shape allows not only unlimited propagation modes along forward and backward directions but also trapped modes because of its unbounded shape. If the light interacts with the hyperbolic media, the scattered mode with ultra-high-k can propagate, while dielectric cannot support high mode index due to its bounded isofrequency curves in circular or elliptical shape. These characteristics have exhibited several advances not only as substrates that enhance local density of states coupled with emitters but also as lenses that enable deep subwavelength resolutions [42, 43]. Especially, HMM waveguides or resonators presented wavelength-independent mode propagation along negative direction and ultracompact light trapping in arbitrary object size [44].

The light interactions with abovementioned materials give insight into various approach for required function in CIS. In this thesis, those materials will be applied for metasurface design including color filter, color splitter, and light trapping.

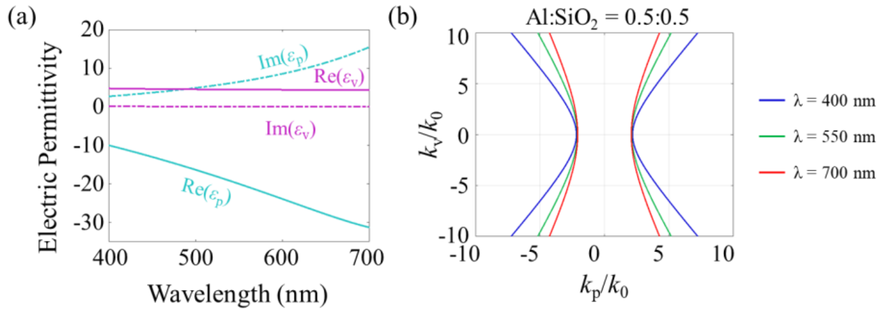

Figure 2.5 (a) Effective permittivity of alternatively vertical stack of Al-SiO_2. (b) Isofrequency curves of Al-SiO2 stack in visible wavelength range.

Chapter 3. Absorptive metasurface color filter based on hyperbolic metamaterial for noise reduction

Metasurface color filters (MCFs) have attracted considerable attention thanks to their compactness and functionality as candidates for optical elements in miniaturized image sensor. However, conventional dielectric and plasmonic MCFs that have focused on color purity and efficiency cannot avoid reflection in principle, which degrades image quality by optical flare or ghost image. Here, I introduce absorptive-type MCFs through truncated-cone hyperbolic metamaterial (HMM) absorbers. Applying particle swarm optimization method to design multiple parameters simultaneously, the proposed MCF is theoretically and numerically demonstrated in perceptive color on CIELAB and CIEDE2000 with suppressed-reflection. Then, color filter array is numerically proved in 255 nm of sub-pixel pitch.

3.1 Introduction

Metasurfaces have been developed to replace conventional color filters in CMOS image sensor in various method such as subwavelength hole or rod arrays [18]. Even if reflection-mode color filters have been reported with high resolution, saturated color purity, and high reflection efficiency with dielectrics by group resonance and second Kerker effect, the architecture of image sensors requires transmission-mode color filters [45-47].

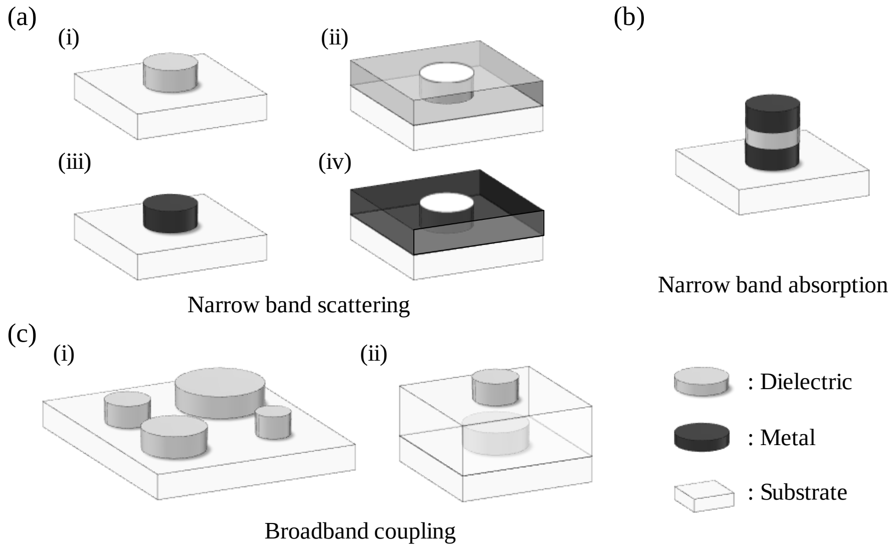

Figure 3.1 Examples of subwavelength unit-cells that have been employed depending on functions. (a) Rods (i, iii) and apertures (ii, iv) composed of dielectric (i, ii) and metal (ii, iv) for narrow band scattering. (b) Metal-dielectric-metal structure for narrowband absorption. (c) Spatial multiplexing of multiple rods for broadband coupling.

Among a number of approaches to polarization independent transmissive metasurface color filters (MCFs), there are two representative design methods based on resonance effect. One is extraordinary optical transmission (EOT), which enables high color purity at plasmonic resonance through subwavelength aperture arrays on metal film as shown in (iv) of Figure 3.1(a) [48]. By manipulating aperture size and period, resonant transmission wavelength can be controlled. The other design method is Mie-resonance that reflects light and partially absorbs light at multipolar resonances of subwavelength antennas based on dielectric metasurface as described in (i) of Figure 3.1(a). It showed apparent advantages in transmission efficiency but has relatively low color purity compared with plasmonic MCFs. For example, the peak transmissions of plasmonic MCFs are (R, G, B) = (< 20 %) in ref. [49] and (R, G, B) = (> 80 %, > 70 %, > 60 %) in ref. [50] but the peak transmissions of dielectric MCFs are (C, M, Y) = (90 %, 90 %, 90 %) in ref. [51] and (R, G, B) = (90 %, 60 %, 50 %) in ref. [52], where R, G, B, C, M, and Y denote red, green, blue, cyan, magenta, and yellow, respectively. Still, it is unpractical that most of transmissive MCFs have not considered reflections that might lower image quality, giving rise to flare effect or ghost image by multiple reflection in CMOS image sensor [53]. Although the light is absorbed at Mie-resonance of amorphous silicon rods, it is not enough to suppress reflection because of low extinction coefficient at green and red wavelength bands [54]. Thus, to circumvent the aforementioned drawbacks of dielectric rods and plasmonic holes, absorption-based MCF with suppressed reflection is indisputably required that functions like conventional pigment or dye color filters.

The candidate of meta-atom needs to meet broadband coupling in visible wavelength but narrowband absorption except desired color spectrum, simultaneously. The typical subwavelength antenna structure for narrowband absorption is metal-dielectric-metal (MDM) composition as depicted in Figure 3.1(b). The light interaction with MDM antenna induces parallel magnetic dipoles by current loop between upper and lower plasmonic rods and absorbs light by loss of metal. Meanwhile, broadband coupling has been realized by spatial multiplexing like Figure 3.1(c). The integration of various sizes of meta-atoms causes wavelength-multiplexing metasurface since each meta-atom modulates the light in narrow-band but whole metasurface operates as broadband metasurface.

Herein, I propose absorptive MCF that is based on truncated-cone HMM waveguide absorbers that operate as a bandstop filter at undesired wavelengths. The truncated-cone HMM waveguide consists of several layers of metal-dielectric films with tapered angle. In a design of spectral response of the truncated-cone HMM waveguide, it looks elusive to decide not only the number of layers, metal filling ratio, and thickness that relate quality of effective medium but also widths of bottom and top of truncated-cone that relate resonance wavelengths. Thereby, I investigate geometry parameters for high figure of merit using particle swarm optimization (PSO) method which is stochastic optimization method in suggested range. The optimized waveguides at blue, green, and red colors are examined in color details, incident angle dependency, and expected color acceptance of virtual CMOS image sensor. Furthermore, amorphous silicon substrate is considered to emulate photodiode of CMOS image sensors. In the last section, the feasibility of MCF array in 255 nm of sub-pixel pitch is demonstrated with potential fabrication process.

3.2 Principle of hyperbolic metamaterial absorbers

Approach to HMM building block begins with cylindrical HMM waveguide composed of alternative stacks of Al-SiO_2 as shown in Figure 3.2(a), investigating effective mode index and power flow along propagation direction at the wavelengths of 400, 550, and 700 nm. The effective refractive mode indices are calculated from characteristic equation as follows [39]:

$$\begin{aligned}&\varepsilon_v f_0\left(\kappa_0 a/\eta\right) = g_0\left(\kappa_0 a\right),\\&\eta = \sqrt{-\varepsilon_p/\varepsilon_v},\\&\kappa = \sqrt{\beta^2 - \varepsilon_p k_0^2},\end{aligned} \tag{3.1}$$

where radius a, $f_n = J_n'(x)/xJ_n(x)$, and $g_n = -K_n'(x)/xK_n(x)$.

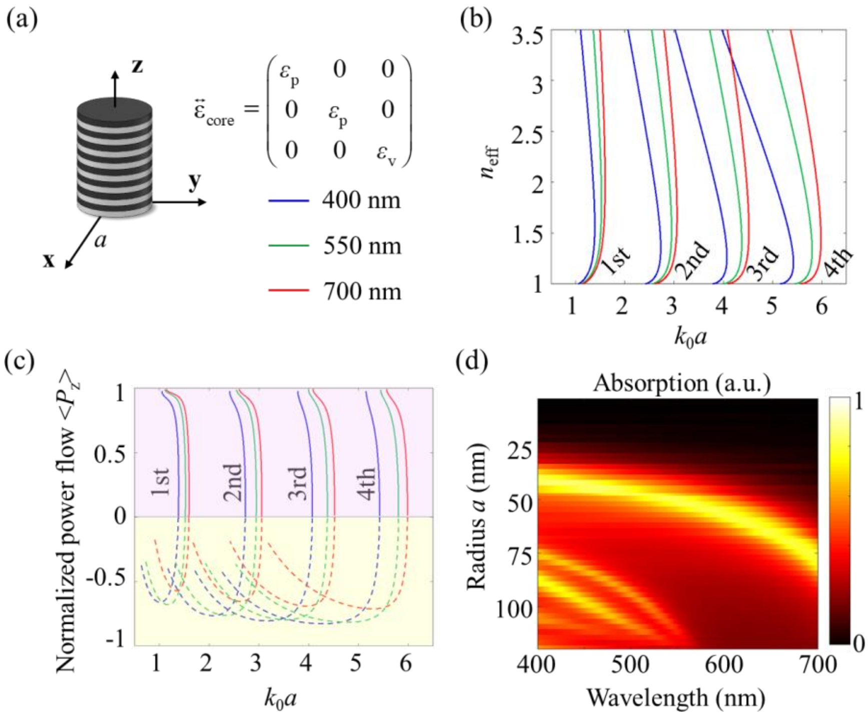

Figure 3.2 (a) Schematic diagram of effective cylindrical HMM waveguide. (b) Effective refractive index along reduced radius (k_0a) calculated by characteristic equation at 400 nm (blue), 550 nm (green), and 700 nm (red). (c) Power flow along propagation axis. Solid lines (light purple box) and dashed lines (light yellow box) denote forward and backward modes, respectively. (d) Absorption spectrum for wavelength and radius.

As mentioned in Chapter 2, Figure 3.2(b) verifies that propagation modes always exist in several bands unrelated to varying object size thanks to unbounded isofrequency curve. As waveguide modes, normalized power flow in Figure 3.2(c) shows light propagation direction of which the solid lines and dashed lines denote forward and backward direction, respectively. Furthermore, the light is trapped at the point of sign change boundary at $\langle P_z \rangle = 0$. The results correspond to absorption spectrum for 500 nm length waveguide in Figure 3.2(d), which is simulated from 3D electromagnetic finite-difference time-domain (FDTD) simulator. As shown in Figure 3.2(d), absorption resonance shifts from 400 nm to 700 nm in increasing radius. For broadband absorption, it is advantageous to vertically spatial multiplexing the various size of cylindrical HMM waveguide because of pixel minimization. This corresponds to vertically-tapered cylindrical HMM waveguide that can absorb broadband lights.

3.3 Absorptive color filter design based on particle swarm optimization method

Figure 3.3(a) explains that a schematic of the proposed metasurface is composed of 12 layers of Al-SiO_2, each of which has 50 nm thickness, sitting on 100 nm-thick SiO_2 spacer (h_{sp}) and Si substrate. To begin with, validity of the proposed structure is determined. One is thermal expansion in terms of layer thickness by absorption heat-up, where the linear thermal expansion along vertical direction is less than 3 nm for 600 nm-thick aluminum in varying the temperature from -20 °C to 200 °C [55]. Also, the contribution of multiple reflection in SiO_2 spacer to optical flare effect is investigated by Eq. (3.2) using scattering matrix method as described in Figure 3.3(b).

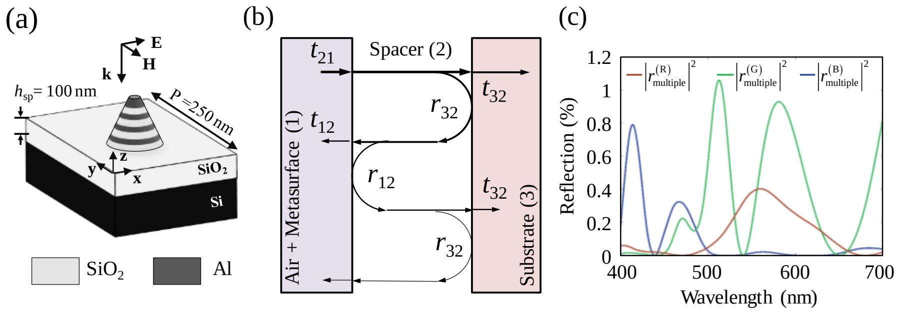

Figure 3.3 Proposed metasurface and optimization process. (a) Unit-cell diagram composed of alternative Al-SiO_2 layers with 100 nm-thick silica spacer on silicon substrate and variable filling ratio. Light is normally incident with polarization-independency. (b) Scattering process in proposed MCF consisting of metasurface (layer 1), SiO_2 spacer (layer 2), and Si substrate (layer 3). (c) Intensity of multiple reflection inside spacer for RGB color filters.

$$\begin{aligned} t_{31}^{(j)} &= t_{32}^{(j)}\{t_{21}^{(j)}\exp\left(in_2k_0d\right)+t_{21}^{(j)}r_{32}^{(j)}r_{12}^{(j)}\exp\left(3in_2k_0d\right) \\ &\qquad +t_{21}^{(j)}\left(r_{32}^{(j)}r_{12}^{(j)}\right)^2\exp\left(5in_2k_0d\right)+H.O.\} \\ &= t_{32}^{(j)}\left\{t_{21}^{(j)}\exp\left(in_2k_0d\right)+\frac{t_{21}^{(j)}r_{32}^{(j)}r_{12}^{(j)}\exp\left(in_2k_0d\right)}{1-r_{32}^{(j)}r_{12}^{(j)}\exp\left(2in_2k_0d\right)}\right\}, \\ r_{multiple}^{(j)} &= \frac{t_{21}^{(j)}r_{32}^{(j)}r_{12}^{(j)}\exp\left(in_2k_0d\right)}{1-r_{32}^{(j)}r_{12}^{(j)}\exp\left(2in_2k_0d\right)},\ j\in\{R,G,B\}, \end{aligned} \tag{3.2}$$

where d denotes spacer thickness. To investigate multiple reflection in SiO_2 spacer, second and high order terms (H.O.) are calculated which are the sum of multiple reflection terms r_{multiple} inside SiO_2 spacer. From the FDTD simulation, I get the scattering matrix sets t_{21}, t_{32}, r_{12} for red, green, and blue color filters. It is noted that intensity of multiple reflection by spacer is under 1.2 % as shown in Figure 3.3(c). Thus, multiple reflection at the boundary of SiO_2 spacer does not affect optical flare effect much.

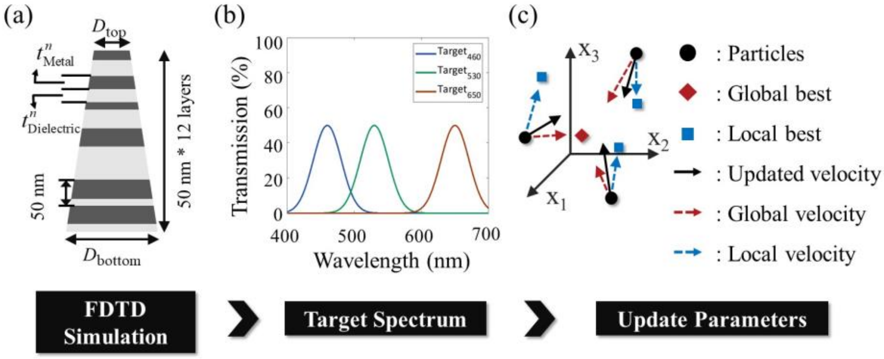

Figure 3.4. Optimization process. (a) Unit-cell diagram composed of 12 Al-SiO_2 layers with variable filling ratio in FDTD simulation. (b) Gaussian lineshape for target center wavelengths of 460, 530, and 650 nm with 50 % efficiency. (c) A schematic of particle swarm optimization. Particle, M-dimensional coordinate, and particle position correspond to FDTD simulation, parameter space, and optimized parameters, respectively.

In design method, absorption range depends on top diameter (D_{top}) and bottom diameter (D_{bottom}) of the tapered HMM. However, since incident light is absorbed wavelength-continuously with uniform ratio of Al-SiO_2 building block, adjusting only D_{top} and D_{bottom} is insufficient to achieve high quality of color from identical meta-atom array. In addition, it is difficult to transmit target colors with suppressed reflection in few degrees of freedom. Taking this into account, I make use of different metal filling ratio $f_n = t^n_{\text{Metal}} / \left(t^n_{\text{Metal}} + t^n_{\text{Dielectric}} \right)$ about every layer for qualitative design. Furthermore, period is minimized to reduce pixel size maintaining low reflection. Since in-plane coupling determined by the longest diameter corresponding to 700 nm resonance and the lattice resonance by the period contribute to reflection, the period reduction is limited [56]. Considering those limitations, the unit-cell structure is arranged in 250 nm period along *x*- and *y*-directions and exhibits no diffraction.

To maximize transmission efficiency and minimize reflection, PSO algorithm is employed. Although deep learning has been applied to achieve exceptional performance in designing complex shape of antennas, it requires huge dataset [57]. Meanwhile, gradient descent algorithm needs to differentiate loss function about all parameters in each iteration. Thus, stochastic algorithms might be more efficient alternatives for the case of large amount of parameters. In electromagnetic simulation based on PSO, each solution with randomly generated parameters in M-dimensional parameter space (x_1, x_2, …, x_M), which is called particle, is solved and moves along better fitness [58]. In our metasurface optimization, members of parameter space are diameters (D_{bottom}, D_{top}) of tapered cylindrical HMM waveguide and metal filling ratio f_{n} of each layer described in Figure 3.4(a).

In an iteration of optimization, randomly-distributed twenty particles are solved using FDTD simulation. From transmission and reflection spectra, loss function is calculated that needs to be minimized. The loss function is defined as sum of L_2 loss between transmission spectrum and Gaussian lineshape as shown in Figure 3.4(b), and one between reflection and zero as shown in the following equation:

$$\begin{gathered} Loss = \frac{1}{N}\left(\sqrt{\sum_{\lambda_{min}}^{\lambda_{max}} \left| T(\lambda) - \eta T_G(\lambda) \right|^2} + \sqrt{\sum_{\lambda_{min}}^{\lambda_{max}} \left| R(\lambda) \right|^2} \right), \\ T_G(\lambda) = \exp\left[-\frac{(\lambda - \lambda_{center})^2}{2\sigma^2} \right],\ \sigma = \frac{\mathrm{FWHM}}{2\sqrt{2\ln 2}}, \end{gathered} \tag{3.3}$$

where N is wavelength sampling number in FDTD simulation. At the loss function of transmission part, I target 50 % of efficiency η and 50 nm of full-width at half-maximum (FWHM), and center wavelengths are 460 nm for blue, 530 nm for green, and 650 nm for red. Next, particles are moving toward minimum loss among all particles and minimum loss of own, which are called global best and local best, respectively as illustrated in Figure 3.4(c). This optimization process is iterated for each metasurface in following sections.

3.4 Numerical analysis on optimized metasurface color filters

3.4.1 Single color filter optimization

Through 100 iterations for each color, I obtain three unit-cells, corresponding to each metasurface for RGB colors. Transmission and reflection spectra in Figures 3.5(a)–3.5(c) are numerically calculated from optimized geometry in Figures 3.5(d)–3.5(f). The details of geometry for each color are given in Table 1, where filling ratio 1 means there is only metal in one layer and 0 means only dielectric. Figures 3.5(a)–(c) verify that transmission spectra reach the maximum near target wavelength and slightly suppressed-efficiency. Reflections are lower than 10 % in total visible wavelength range but this is negligible even if multiple reflections between MCF and other optical elements in CMOS image sensor exist (< 1 %).

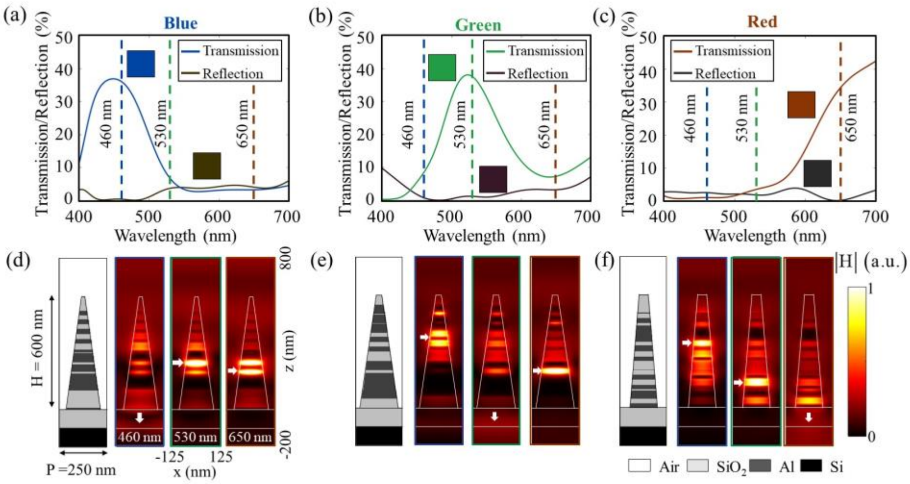

Figure 3.5 Transmission and reflection spectra from optimized metasurface for (a) blue, (b) green, and (c) red color. Insets in (a–c) depict perceptual colors from CIELAB. Dashed lines at 460 nm, 530 nm, and 650 nm indicate center wavelengths of target spectrum. (d)–(f) *XZ* cross-sections of enlarged optimized meta-atoms and normalized electric field at target wavelengths. White dotted lines denote boundary of meta-atom and substrate. White arrows indicate the spatial position of electric field resonances excited by meta-atom and transmitted light.

Table 3.1. Optimized geometry parameters for MCF

Color	Geometry Parameters													
	D_{bottom} (nm)	D_{top} (nm)	Metal Filling Ratio in Bottom to Top Order											
Blue	185	20	0.11	0	1	0.81	0.78	0.96	0.31	0.47	0.54	0.53	0.44	0
Green	204	34	0	1	1	0.69	0.98	0	0.52	0.56	0.94	0.91	1	0
Red	147	53	0.49	0.84	0.42	0.50	0.03	0.42	0.65	1	0.71	0.51	0.11	0

To demonstrate that the given metasurfaces operate as absorptive MCFs, normalized electric field distributions are examined under linear polarization illumination. At the wavelength of dashed lines in blue color at 460 nm, electric fields propagate through substrate. Meanwhile, the light is confined at the respective resonant positions at 530 nm and 650 nm in Figure 3.5(d). Likewise, light passes through meta-atom at each target wavelength of green and red color filters but is confined at unwanted wavelengths in Figures 3.5(e) and 3.5(f). Then, light is absorbed because the confined light is dissipated by loss of metal.

Provided that these color filters are used for CMOS image sensor, it can be expected that how colors are recognized by suggesting CIELAB color space (L^*, a^*, b^*) [59]. The CIELAB expresses luminance of light spectrum and represents colors considering human's non-uniform vision perception, whereas CIE 1931 coordinate describes only chromaticity from normalization of CIEXYZ [60]. The equations to calculate CIELAB is given in Appendix A.1. The optimized color filters in CIELAB space result in blue, green, and red colors for transmission spectra and almost dark brown and black colors for reflection spectra as rendered in inset of Figures 3.5(a)–3.5(c) and Figure 3.6. The CIELAB values (L^*, a^*, b^*) of transmission are (31.4, 21.2, -56.4), (56.9, -51.5, 35.7), and (34.2, 34.5, 44.2) for blue, green, and red color filters, respectively. Meanwhile, CIELAB values of reflection colors are (22.0, -1.35, 30.0), (13.6, 18.1, -3.8), and (17.3, 0.622, -0.181) for blue, green, red color filters. It can be seen that RGB colors in transmission spectra achieve much higher chromaticity and larger lightness than reflection spectra. In particular, in Figures 3.6(a) and 3.6(b), the reflection colors are concentrated on axis in L^*a^*, L^*b^*, and a^*b^* coordinates, which means their chromaticity approaches zero. Furthermore, the RGB colors are farther from center than reflection colors in Figure 3.6(b). As perspective on figure of merits (FoMs) about transmission per reflection spectra, the ratio between summed-square-magnitude of transmission and one of reflection in visible range is examined in Figure 3.6(c). It is noted that FoM is achieved higher than 14.63 dB for all color filters, which means high quality color filter with suppressed reflection.

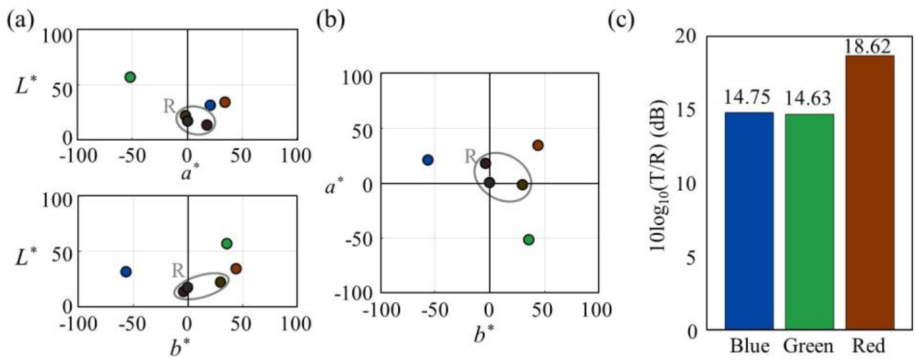

Figure 3.6 Colors calculated from CIELAB space. Transmission and reflection spectra correspond to each point and color on (a) L^*a^* and L^*b^* coordinates, and (b) a^*b^* coordinate. The points in gray ellipse represent reflection colors. (c) Transmission and reflection ratio.

3.4.2 Angle tolerance for optimized metasurface color filters

We turn to illumination condition in Figure 3.7. It is important to maintain performance about oblique incidence in CMOS image sensors. Unlike the conventional color filters composed of pigment or dye, MCFs depend on incident angle by nanostructure array. Illuminating light from 0 to 40 degrees of incidence angle in transverse electric (TE) and transverse magnetic (TM) waves as depicted in Figures 3.7(a) and 3.7(d), chromaticity variation of transmitted light is shown along black arrow direction with inclement of 5 degrees on a^*b^* coordinate in Figures 3.7(b) and 3.7(e). In addition, to quantitatively analyze lightness and chromaticity variation from original color, I suggest advanced color difference metric CIEDE2000 (ΔE_{00}) [61]. The details of CIEDE2000 calculation method are explained in Appendix. The color modification based on CIEDE2000 is analyzed in Figures 3.7(c) and 3.7(f). It is known that color difference is noticeable at condition of $\Delta E_{00} < 3$ and appreciably noticeable at $3 < \Delta E_{00} < 6$ [62]. Thus, note that the optimized color filter is consistent in consideration of $\Delta E_{00} < 3$ with respect to oblique incident angle.

For TE wave, Figure 3.7(b) indicates little chromaticity variation for blue and green color filters, but relatively larger shift for red color filter. The blue color shifts to deep blue and purple, the green color almost stays, and the red color moves toward blue which loses the chromaticity. From the color difference in Figure 3.7(c), the colors are maintained until 20 degrees for the green, and 15 degrees for the blue color filters. And the ΔE_{00} about the red color filter is not more than 3 until 40 degrees. In comparison with low chromaticity variation in Figure 3.7(b), the major color difference is caused by lightness degradation for TE case.

On the other hand, it seems that chromaticity for TM wave decreases but lightness becomes brighter in Figure 3.7(e). The blue and red colors are shifted toward bright cyan and bright red, respectively. Meanwhile, the green color is shifted toward bright green. The color difference in Figure 3.7(f) illustrates that blue, green, and red color filters are consistent under 10 degrees, 15 degrees, and 13 degrees, respectively.

In comparison with TE and TM incidence, the color differences for TM wave are more affected than TE wave. This is because tangential electric field excites tangential electron oscillation at resonant wavelength but the effective wavelength of tangential electric field is reduced with incident angle of TM wave increasing. In both TE and TM waves, the color differences increase with the incident angle increase. This is because incident wave couples with meta-atom by effectively small cross-section. In addition, shorter wavelength gives rise to diffraction with incident angle increasing, where the 1st diffraction order exists from 5.06 degrees at 400 nm to 49.9 degrees at 643 nm.

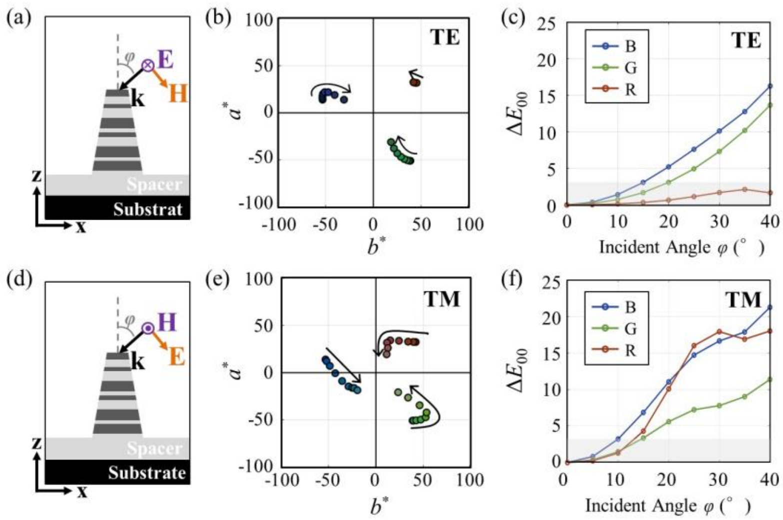

Figure 3.7 Incident angle dependence in terms of polarization of (a-c) TE modes and (d-f) TM modes. (a, d) Schematic diagrams of TE and TM incidence. (b, e) Chromaticity variation in a^*b^* coordinates. The dots are distributed in increase of 5 degrees along black arrows. (c, f) Color difference expressed by CIEDE2000 from CIELAB with respect to incident angle. The light gray boxes denote just-noticeable region.

3.5 Sub-micron metasurface color filter array

Until now, optimized meta-atom is arranged in period about each color filter. However, absorptive metasurface color filter array (MCFA) is designed to glimpse a feasibility of our proposed method on conventional RGB sub-pixel array. Since every color pixel shares vertical geometry parameters such as metal filling ratio, thickness of each layer, and number of total layers, optimization based on single meta-atom is restricted for three colors simultaneously. Accordingly, I design each color by spatially multiplexing meta-atoms in 2 x 2 Bayer arrangement as shown in Figure 3.8(a). For normal incident of transverse electric (TE) and transverse magnetic (TM) waves, Bayer MCFA is optimized about whole geometry parameters of RGB sub-pixel simultaneously including top/bottom widths, sub-pixel pitch, thickness and filling ratio of each layer in each color pixel. The boundary conditions are set to periodic condition along *x*- and *y*-direction and perfectly matched layers (PMLs) along *z*-direction. To increase the degree of freedom, the number of layers is selected as 15.

Table 3.2. Optimized geometry parameters for metasurface color filter array

Color	Blue	Green	Red
D_{bottom} (nm)	143	75	240
D_{top} (nm)	21	30	20
Layer thickness (nm)	(53, 25, 27, 70, 60, 20, 70, 70, 20, 20, 70, 20, 70, 70, 27)		
Metal filling ratio	(0.2, 0, 0, 0.78, 1, 0.27, 1, 1, 0, 1, 0.73, 1, 0.96, 1, 0)		
Sub-pixel pitch (nm)	255		

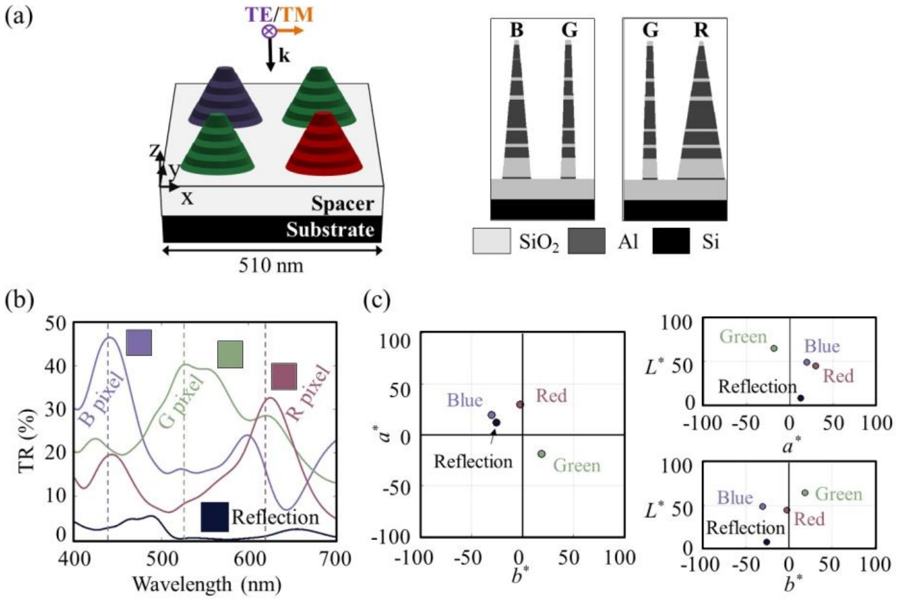

Figure 3.8 (a) Schematic diagram of MCFA and material distribution at the cross-section of each meta-atom. (b) Transmission and reflection spectra from optimized MCFA for entire RGB pixel. (c) Color distribution on CIELAB space.

Since I assume that all transmitted power is absorbed by photodiode, transmission power is measured at the boundary of spacer and Si substrate and averaged for incident transverse electric and transverse magnetic waves. By particle swarm optimization, geometry parameters are given in Table 3.2 and described in Figure 3.8(a). The order of layer thickness and metal filling ratio in Table 3.2 is bottom to top layer. Transmission spectra of each color filter and reflection spectrum of whole Bayer pattern are given in Figure 3.8(b). From this spectra, Figure 3.8(c) shows the color distribution of optimized MCFA. The luminance L^* is higher than single MCF in Figure 3.5 but the chromaticity is lower than single MCF due to spectral broadening caused by diffraction orders and in-plane coupling between meta-atoms.

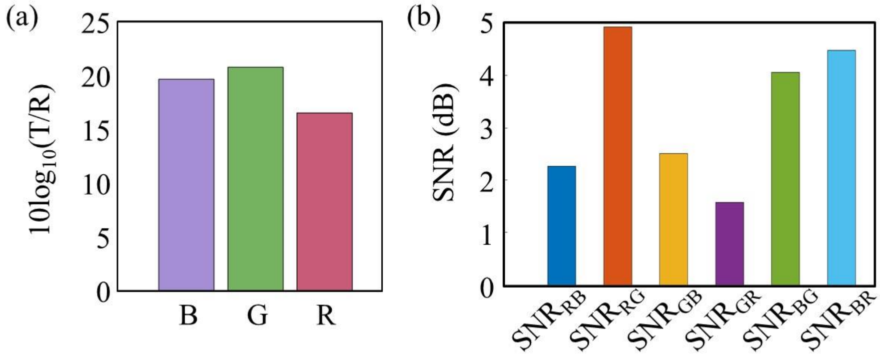

Figure 3.9 (a) Transmission-reflection ratio about Bayer pattern MCFA. (b) The SNRs among colors in each color pixels.

To quantitatively identify MCFA, SNRs for transmission-reflection ratio (TRR) and color crosstalk are investigated. As shown in Figure 3.9(a), the TRRs for RGB pixel are higher than 17 dB, which means reflection noise is suppressed. On the other hand, SNR for color crosstalk between target color and undesired color which is originated from direct transmission and diffraction from neighboring pixels is calculated as follows:

$$SNR_{ij} = 10\log_{10}\left(\int_i d\lambda T_i \Big/ \int_j d\lambda T_i\right),\ \left(i, j = R, G, B\right), \tag{3.4}$$

where T_i denotes transmission spectrum of target color pixel and T_j denotes transmission spectrum of unwanted color in target color pixel. The integration ranges of R, G, and B are 60 nm-width from the center of the wavelength of peak transmission of each color, which are 435 nm, 530 nm, and 625 nm. In the Figure 3.9(b), the SNR of red is high with respect to green and low with respect to blue. And the SNRs of green to blue and red are low. But SNRs of blue to red and green are high. This means that SNR tends to follow the inverse of spectrum broadening of each pixel. Since most of color interference is caused by diffraction from neighboring pixel, I believe that this color crosstalk can be overcome by isolation trench or lens-array in modern image sensor [63].

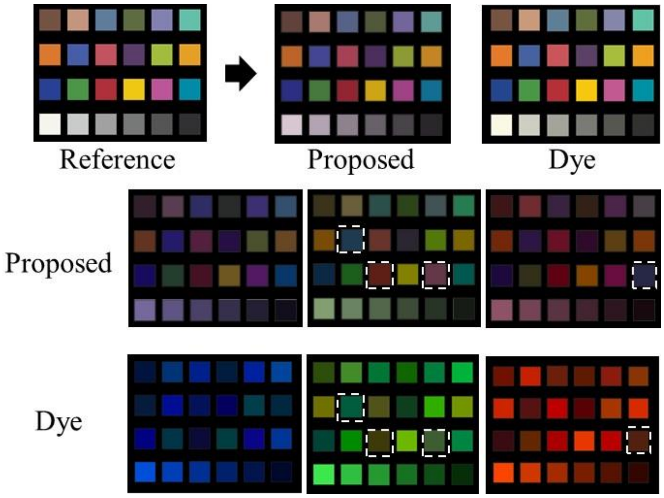

Figure 3.10 Color simulation from Gretag-Macbeth color chart for single MCFs and Bayer MCFA. The white dashed squares denote calculated color by the proposed MCFA and conventional dye color filters.

Here, I inspect the image quality captured by MCFs. Figure 3.10 assumes that the designed MCFs are integrated with CMOS image sensor and Gretag-Macbeth chart is measured as reference colors. The image is reproduced by integration of transmission efficiency passing through each MCF in Figure 3.5 and MCFA in Figure 3.8. The transmission efficiency of each color is measured by power monitor at the boundary of SiO_2 spacer and Si substrate for plane-wave incidence with elemental spectra of Gretag-Macbeth chart. The average and standard deviation of ΔE_{00} are 15.53 and 4.217 for MCFs, but 9.43 and 2.7 for MCFA, respectively, where lightness accounts for most part of ΔE_{00}. Although there are the color differences, it seems that the color tolerance can be corrected by exploiting white balance, color correction matrix, and gamma correction in practical CMOS image sensors [61]. From the blue, green, and red color filters, each element of color chart is shown in Figure 3.10. Since the color crosstalk of green color filter on red region, the comparison of white dashed squares between the proposed and dye color filters shows more reddish colors for the proposed color filters.

Furthermore, I expect that our proposed MCFA can be fabricated by focused ion beam (FIB), where fabrication error is simulated in Figure 3.11. I briefly discuss a potential fabrication method to manufacture the proposed MCFs. Although electron beam lithography has an advantage in fabricating large-scale metasurface, the geometry condition of vertically tapered and multiple-layered Al-SiO_2 meta-atom looks very challenging. The focused ion beam can be attributed to control tapered angle and fabricate metal-dielectric simultaneously, which is manipulated by using grayscale exposure dose [64].

First, aluminum and silica films are alternatively deposited by e-beam evaporator and atomic layer deposition, respectively, in consideration of accuracy of layer thickness. And then meta-atom array is patterned by FIB based on predefined grayscale map as depicted in Figure 3.11(a). To predict fabrication reliability, I investigate how geometric deviations influence color distortions, where the deviations include individual layer-thickness $\tilde{t}_n$, bottom diameter D'_{bottom}, top diameter D'_{top} in Eq. (3.5), and rounded-tip.

$$\begin{aligned} D'_{bottom} &= D_{bottom} + \delta_{bottom}, \\ D'_{top} &= D_{top} + \delta_{top}, \\ t'_n &= t_n + \delta_n, \left(n \le 12, n \in \mathbb{N}\right) \end{aligned} \tag{3.5}$$

where δs are errors of geometric parameters and n denotes n-th layer of the proposed MCFs. The thickness error means variation of individual layer thickness, not total thickness of MCFs. In Figure 3.11(b), calculated color distribution on CIELAB is given by 180 simulations of which geometric parameters are randomly selected in the range from -10 to 10 nm for δ_{bottom}, δ_{top}, and δ_n. To quantitatively evaluate fabrication error, standard deviations of (L^*, a^*, b^*) are (3.44, 12.3, 6.15), (5.24, 7.44, 14.0), and (8.45, 6.58, 11.3) for blue, green, and red color filters, respectively. As examples of fabrication error, color table is illustrated in Fig. 10(c). It shows that colors present still their own colors in about 20 nm (-10 to 10 nm) of diameter tolerance and about 20 nm of thickness tolerance (-10 to 10 nm).

Lateral errors can be manipulated by exposure dose calibration using commercial focused ion beams from Zeiss and FEI Co. that have 3 nm resolution. Meanwhile, vertical errors could be expected, determined by deposition-uniformity, which is less than 5 % for commercial e-beam evaporators from Rocky Mountain Vacuum Tech Inc. and less than 1 nm-roughness for atomic layer deposition [65]. In addition, the influence from rounded-tip is not much critical as shown in Figure 3.11(d). I set the geometry of top layer to paraboloid. There is little spectral variation for blue and red MCFs but enhanced transmission response for green MCF. Thus, the proposed fabrication method can be one fabrication method.

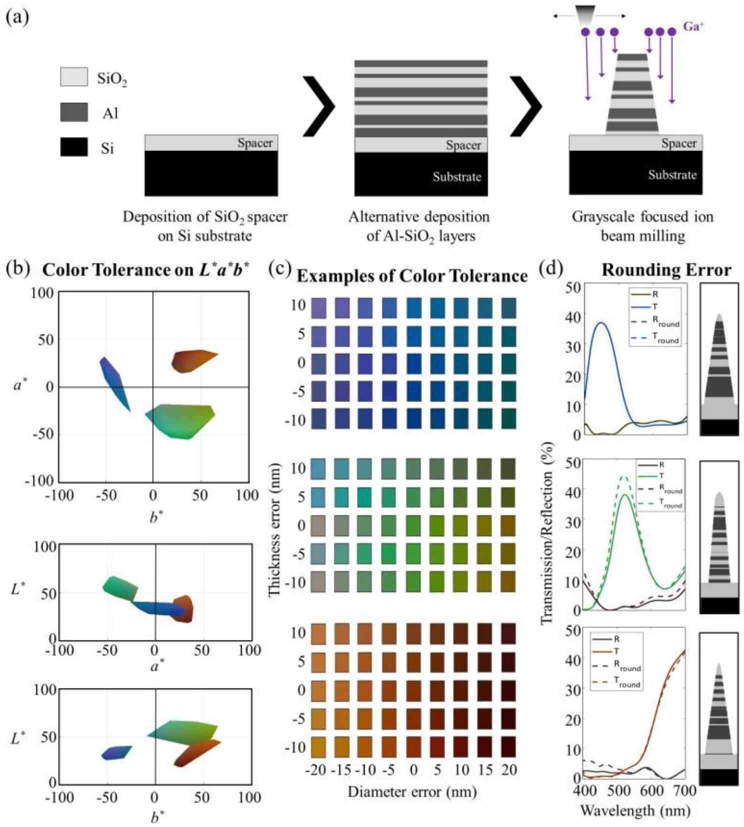

Figure 3.11 (a) Fabrication process. The SiO_2 spacer is deposited and Al-SiO_2 layers are alternatively deposited. And then FIB milling is performed by Ga^+ ion. (b) Color tolerance by geometric fabrication error for randomly distributed error from -10 to 10 nm of individual layer-thickness and bottom/top diameters. (c) Examples of color tolerance from -20 to 20 nm of bottom/top diameters simultaneously and from -10 nm to 10 nm of all layer thickness. (d) Cross-sections of rounded-tip structure with its transmission and reflection spectra where solid-lines and dashed-lines denote spectra of optimized color filter and with rounding errors.

3.6 Conclusion

In conclusion, I propose and design metasurface for ultracompact color pixels. Distinct from conventional transmissive MCFs that have principally inevitable reflection, absorbers substitute for transmission band manipulation. Theoretical and numerical calculations on cylindrical HMM waveguide provide insight into absorptive MCF. In design method, PSO enables optimization of meta-atom with respect to various parameters simultaneously. Optimized color filters achieve 14.75, 14.63, and 18.62 dB of transmission colors compared with negligible reflection for blue, green, and red color filters, respectively. In comparison with plasmonic MCFs and all-dielectric MCFs, our work produces little reflection and similar transmission with plasmonic MCFs. Using CIELAB, numerical investigation in visual perception of color at D65 environment is examined. It is notable that reflection is suppressed in terms of chromaticity. Moreover, virtual CMOS image sensor based on our proposed MCFs shows consistent image quality for every color of Gretag-Macbeth color chart. As a factor of image degradation, color difference calculated from CIEDE2000 is maintained under 15 degrees of oblique incident angle in both of TE and TM polarization. Finally, I design subwavelength color filters in arrangement with 255 nm sub-pixel pitch for practical application. And grayscale FIB milling can support feasibility of designed metasurface. Therefore, I expect that the proposed metasurface can be a candidate in application to miniaturized CMOS image sensor.

Chapter 4 High-efficient full-color pixel array based on freeform nanostructures for high-resolution image sensor

The chapter 3 demonstrated the absorptive color filter that resemble with conventional color filters. However, it still limits maximum transmission efficiency as 1/3 for RGB pattern. In this chapter, color splitters that realize efficiency excess about conventional color filter will be discussed.

4.1 Introduction

Pixels of color CIS consist of multiple color sub-pixels, which are implemented by pigments or dye molecules arranged in RGGB, RGBW, RYYB Bayer, X-trans, quad Bayer, and nonacell patterns. The pigment or dye molecule operates as bandpass filter but absorbs undesired band. This restricts transmission efficiency of each color as area accounting for single pixel. For example, RGGB Bayer pattern composed of red, green, and blue with 25 %, 50 %, and 25 %, respectively, corresponds to the maximum efficiencies. Thus, this inevitable limitation based on absorption mechanism of color filter requires an alternative solution.

While conventional photodiodes using bulk silicon absorb light without recognizing wavelength in its absorption band, subwavelength anti-Hermitian metasurfaces of which coupling condition enables spatially-divided channel depending on wavelength to sort two or three colors with critical control of geometry and period of silicon nanostructures [66-68]. It has been realized in one-dimensional silicon grating and two-dimensional *p-i-n* silicon diodes. However, this device requires delicate geometry fabrication for anti-Hermitian coupling condition so that limits degree of freedom [66].

On the other hand, diffractive metasurfaces have been reported that split and guide light into sub-pixels in terms of colors. Micron-scale wavelength-resolved metalenses have also been reported by spatial-multiplexed metalens [19]. Since it requires interleaved large-area region with lens-phase distribution and polarization degree of freedom, it is not suitable for miniaturized pixels. As one candidate of sub-micron metasurface for color-dependent focusing, topology-optimized three-dimensional voxel was reported in $(2\ \mu m)^3$ [27]. Although the numerical results showed high transmission efficiency, it was impossible to fabricate in nanoscale. Thus, single-layer and sub-micron scale pixel is highly indispensable.

In 2013, single silicon nitride nano-bar was proposed for resonant diffraction, where one color is diffracted into both of 1^{st} and -1^{st} orders to double efficiency of neighboring color by Panasonic [21]. Recently, NTT suggested nanorod-based metasurface that utilizes dispersive phase modulation leading to RGB colors into 1^{st}, 0^{th} and -1^{st} orders, respectively [28]. However, this results that the device covered only one sub-pixel and added color impurity from direct incident of white light because linear variation of straightforward nanostructure cannot search whole combination of phase gradient about RGB, GBR or BRG distribution. Thus, the challenge here lies in the fact that how to find adequate meta-atom shape without library searching method. Very recently, freeform metasurfaces that are optimized by various methods including topology optimization or evolutionary algorithms have been developed to design high-efficient de-multiplexers [69-72]. The freeform metasurface offers the possibility to design color splitter thanks to large degree of freedom caused by the complex shape. Here, I introduce freeform metasurface full-color splitter based on combination of triple color splitters as shown in Figure 4.1(a). Distinct from conventional silicon nitride metasurface, each metasurface deflects (R, G, B), (G, R, B), and (B, G, R) colors in order of (+1st, 0th, -1st), which are termed RGB, GRB, and BGR, respectively. Hence, integration of optimized color splitters elicits high-efficient color pixels as shown in Figure 4.1(b). For example, red pixel deflects blue light into -1st order and green light into +1st order. So, neighboring blue and green pixels gain another blue light and green light. This is iteratively optimized using rigorous coupled wave analysis (RCWA) with graphics processing units (GPU) in Python 3.7.10 platform.

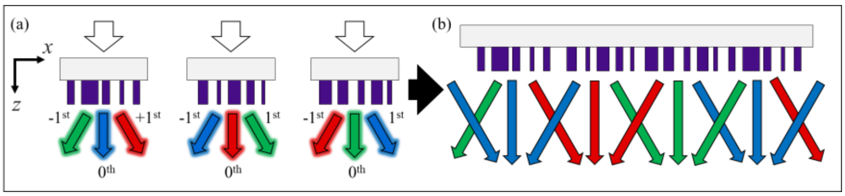

Figure 4.1 (a) A schematic of freeform metasurface full-color splitter for sub-pixel (b) Integration scheme of sub-pixel color splitters.

4.2 Optimization of metasurface full-color splitter

4.2.1 Optimization process

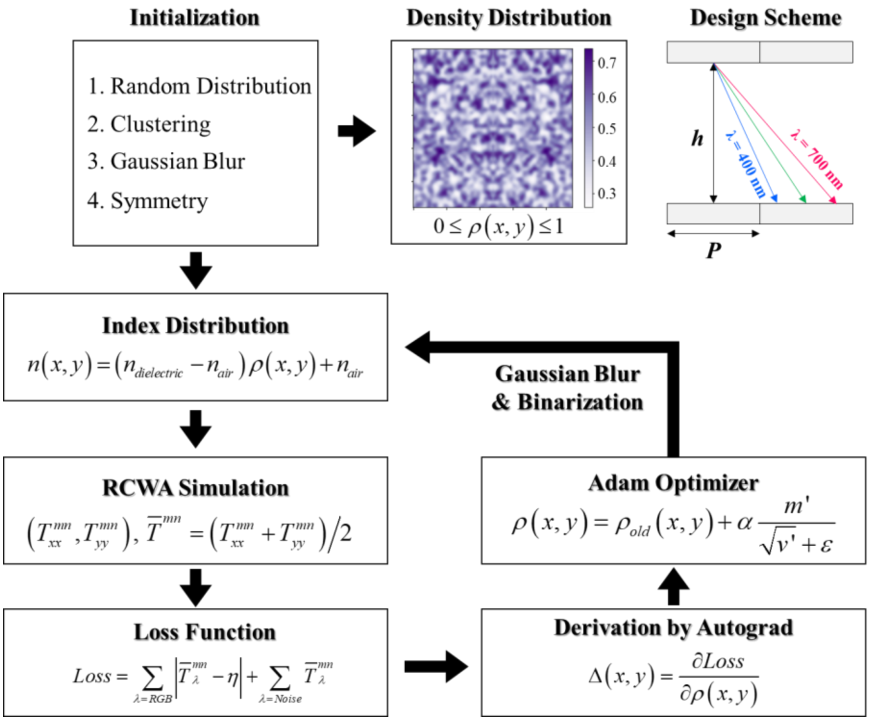

Figure 4.2 Summarized flow chart of optimization process based on gradient of refractive index distribution

Initialization

The inverse design process begins with target simulation space. The simulation space is determined by diffraction angle from 400 nm to 700 nm of wavelengths as follows:

$$P = h \tan\left[\sin^{-1}\left(\frac{\lambda}{P}\right)\right] \tag{4.1}$$

To intend that the deflected colors arrive in neighboring sub-pixels, diffraction angle ranges from 20 to 35 degrees under 1200 nm of period P

along x-direction and corresponding distance h from image sensor to metasurface is about 2330 nm. In this space, initial index density profile $\rho(x,y)$ satisfying $n(x,y)=\rho(x,y)(n_{SiN}-n_{air})+n_{air}$ is suggested by random distribution on 5 nm mesh. Since the initial condition highly affects final-optimized profile in symmetry, hole size or cluster size [73], initial condition is preprocessed by clustering mesh in 25 nm and symmetrizing distribution along y-direction. In addition, Gaussian blur is applied to consider robustness in fabrication [74].

Optimization process

Optimization process consists of RCWA simulation, loss function calculation, gradient calculation, and index density update based on gradient descent method. First, under the given index density profile, transmission is calculated by using RCWA simulation. During the one iteration optimization, x- and y-polarized normally incident conditions at target wavelengths 430 nm (B), 550 nm (G), and 680 nm (R) are successively calculated. And then average transmitted diffraction efficiency of (m, n) orders $\overline{T}_{\lambda}^{mn}=\left(T_{xx,\lambda}^{mn}+T_{yy,\lambda}^{mn}\right)/2$ is utilized for loss function that operates as polarization-independent device. The loss function is defined by the sum of difference between diffraction efficiency and target efficiency η, and untargeted diffraction orders to suppress them in Eq. (4.2),

$$Loss=\sum_{\lambda=R,G,B}\left|\overline{T}_{\lambda}^{target}-\eta\right|+\sum_{\lambda=R,G,B}\overline{T}_{\lambda}^{noise}, \tag{4.2}$$

where the superscript of T denotes diffraction orders. For example, the loss function for diffraction into (1^{st}, 0^{th}, -1^{st}) of BGR metasurface is defined as follows:

$$Loss_{BGR} = \left|T_B^{10} - \eta\right| + \left|T_G^{00} - \eta\right| + \left|T_R^{-10} - \eta\right| \\ + T_G^{10} + T_R^{10} + T_B^{00} + T_R^{00} + T_B^{-10} + T_G^{-10}. \tag{4.3}$$

Then, take the derivative with respect to index density $\rho(x,y)$ by using Autograd in Pytorch library, which is based on chain rule. Throughout the Autograd, complex value differentiation and eigen-decomposition are required and implemented with reference [75]. To update index density, Adam optimizer is applied due to its superior to directionality and momentum correction. The abovementioned process iterates 1000 times. During the iteration, index profile is Gaussian blurred every 200 times to compensate for fabrication difficulty. And then binary push is exploited every 10 times after 600 iterations with slowly increased β in Eq. (4.5).

$$\rho_{bf}(x,y) = \left(\varsigma e^{-\beta(\varsigma-\rho(x,y))/\varsigma} - \left(\varsigma - \rho(x,y)e^{-\beta}\right)\right) \times (\rho \le \varsigma) \\ + \left(1 - (1-\varsigma)e^{-\beta(\rho(x,y)-\varsigma)/(1-\varsigma)} - \left(\varsigma - \rho(x,y)e^{-\beta}\right)\right) \times (\rho > \varsigma). \tag{4.5}$$

Furthermore, target efficiency is empirically determined as 40 %. This is because the refractive index of SiN is lower than silicon resulting in weak field confinement and weak inter-mode coupling that is detailed in section 4.2. It could be low value, but it leads to maximum efficiency of conventional color filter array.

4.2.2 Results and discussion

Color performance

Through optimization, three color splitters are achieved. As shown in Figure 4.3, optimized patterns are Figures 4.3(a-c). Each of them is analyzed by RCWA simulation with high enough Fourier orders and they achieve near 40 % diffraction efficiency in terms of target R, G, and B colors. In Figure 4.3(d-f), diffractions of linearly polarized lights along *x*- and *y*-direction are exhibited, which have little deviation. The colored areas imply highly tolerable in arbitrary-polarized light so that a polarization insensitive function can be allowed.

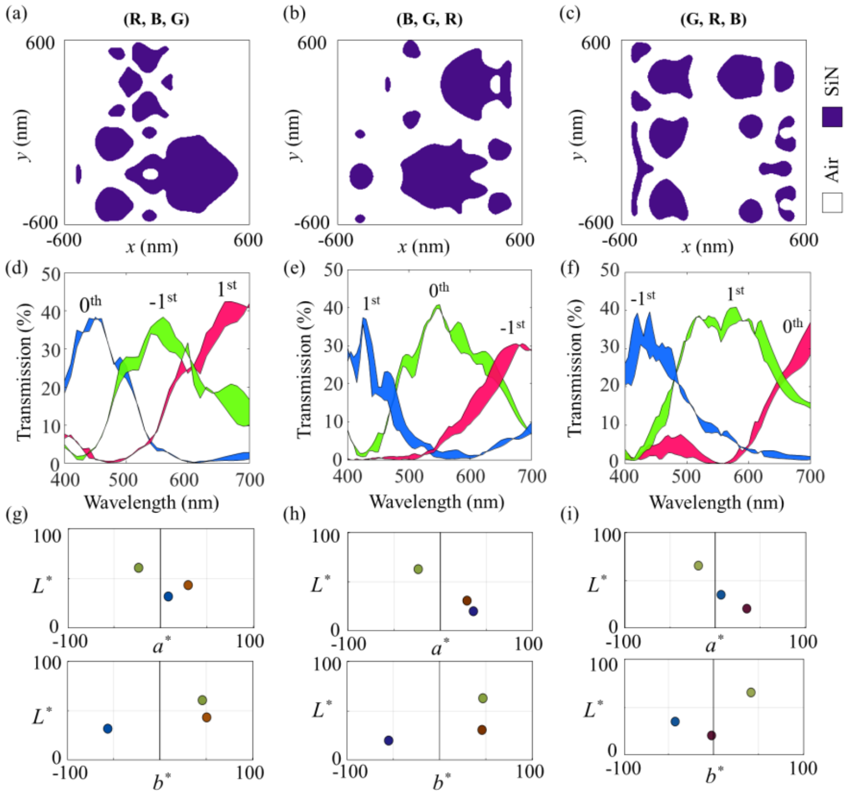

Figure 4.3 (a-c) Optimized freeform metasurface cross-section of RBG, BGR, and GRB in order of (1^{st}, 0^{th}, -1^{st}), respectively. Purple area means SiN distribution. (d-f) Corresponding diffraction efficiencies. Each colored area surrounded by two line-graphs from *x*- and *y*-polarized illumination denotes polarization tolerance. (g-f) Color distribution on CIELAB coordinates with respect to L^*, a^*, and b^*.

From each diffraction efficiency, performance in color splitting is studied on CIELAB coordinate as described in Figures 4.3(g-i), which are numerically derived by the average of diffraction efficiencies with respect to polarization. In L^*a^* and L^*b^* coordinates, the lightness of green color is higher than the other colors. This is more helpful for efficient color sensing similar way that color pixel has two green pixels for twice luminance on purpose. Furthermore, the purity of colors shows much higher than conventional transmission type color filters based on dielectric metasurface [52]. To delineate the performance in color purity, CIE 1931 color gamut, which does not reflect on luminance, is suggested in Figure 4.4. As depicted in Figure 4.4, color coordinates of each diffraction order and their normalized color in rectangular box are suggested. Compared to standard RGB color space which is called sRGB, each metasurface accounts for 41.43 %, 51.62 %, and 34.04 % with exceeding sRGB about 5.71 %, 2.45 %, and 1.46 %, for RBG, BGR, and GRB color splitters, respectively.

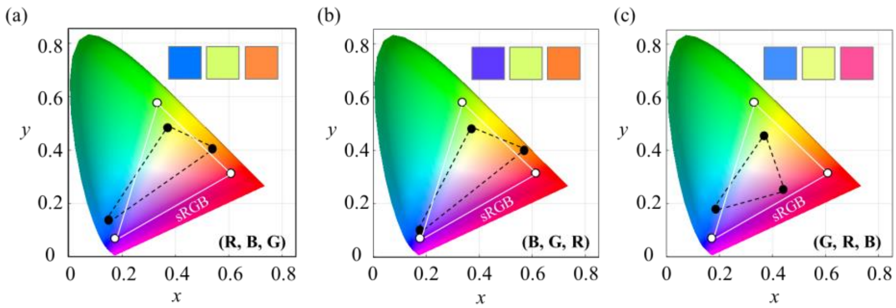

Figure 4.4 Color distribution on CIE 1931 analyzed by diffraction efficiency of (a) RBG, (b) BGR, and (c) GRB metasurfaces.

Physics on freeform metasurface

The periodic freeform metasurfaces can be explained by mode interaction on account of reflection at the boundaries of substrate/metasurface and metasurface/air. In RCWA simulation, the number of Fourier orders corresponds to the number of calculated eigenmodes. However, as shown in Figure 4.5(a), there are not many propagation modes, which contribute to diffraction efficiency in far-field, while eignemodes except the propagation modes are dissipated or near-field radiation. In Figures 4.5(b-f), magnetic field distribution presents eigenmodes that are spatially distributed on different location and intensity. This spatial characteristic gives rise to wavelength-dependent diffraction efficiency and it is induced by optimized freeform shape.

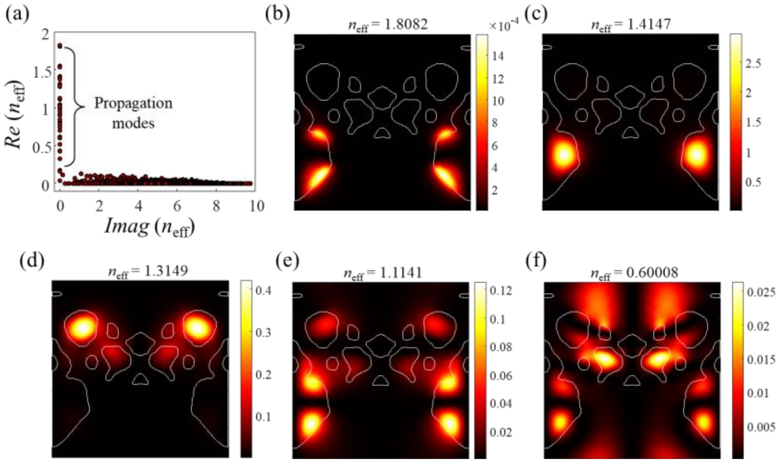

Figure 4.5 (a) Effective refractive indices of eigenmodes in freeform metasurface layer for RBG color splitter at λ = 680 nm. (b-f) Magnetic intensity $|\mathbf{H}|^2$ distributions of propagation modes.

4.3 Implementation of color splitters

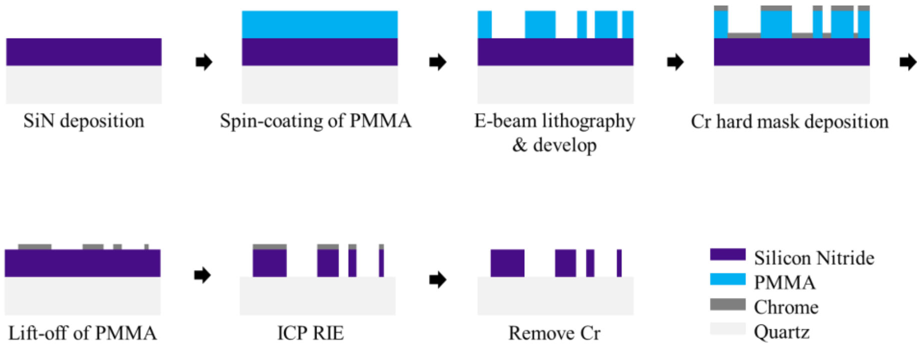

Figure 4.6 Fabrication process of the proposed metasurface that follows traditional e-beam lithography process with ICP RIE.

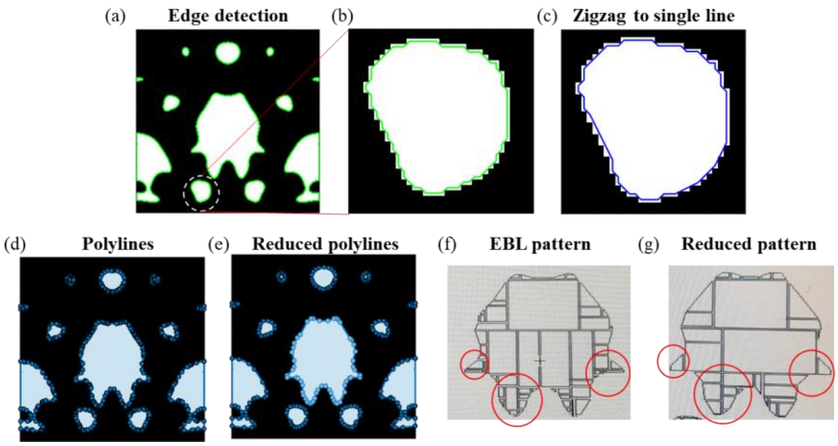

Figure 4.7 Process of GDS file generation for desired freeform pattern. (a) Detected edge of the optimized BGR pattern and (b) its enlarged pattern. (c) Convert zigzag polylines into a single line. (d) Vertices of polylines after (c) and (e) its reduced vertices. (f) Exposure patterns in E-beam lithography from (d) and (g) patterns from (e).

To implement the proposed metasurface, it is fabricated by e-beam lithography process as depicted in Figure 4.6. First 600 nm of silicon nitride is deposited using plasma-enhanced chemical vapor deposition (PlasmaPro System100, Oxford) on quartz wafer. For e-beam lithography, bi-layer e-beam resists (PMMA 495K A4, PMMA 950K A2), and e-spacer are sequentially spin-coated. The e-spacer prevents electron charging through e-beam lithography. The freeform pattern is defined by e-beam lithography (JBX-6300FS, JEOL) in 100 kV condition, and developed by MIBK:IPA 1:3. In e-beam lithography for freeform metasurface, each element is composed of a number of polylines due to curvature of meta-atom arising with memory problem. Thus, the pattern with curvature needs to be approximated for a minimum of lines by pre-processing as shown in Figure 4.7. In detail, the pattern consists of 1,306 of polylines surrounding freeform pattern. To simplify the polylines, the polylines with same gradients reduces to a single line. Then, zigzag lines are converted into a single line as shown in Figure 4.7(c). Next, the patterns are manually designed with 261 of polylines compared in Figures 4.7(d) and 4.7(e). This process results in simplified exposure patterns as displayed in Figures 4.7(f) and 4.7(g).

Furthermore, dose condition is carefully controlled because it affects feasibility of small holes and rods. After e-beam lithography and develop, hard mask is defined by 20 nm-chrome deposition using e-beam evaporator (KVE-3004, Korea Vacuum Tech) and the PMMA removal by acetone in sonicator. Finally, the silicon nitride device is fabricated by inductively coupled plasma reactive-ion etching (ICP 380, Oxford system) during 120 s with SF_6:O_2 = 9:1 with redundant chrome removal by chrome etchant.

The fabricated devices of which total feature size are 480 μm × 480 μm are captured by field emission scanning electron microscope (S-4800, Hitachi) in Figure 4.8(b). Each of samples is fabricated for RBG, GRB, and BGR color splitters. To verify that the light is divided by colors, transmission-type microscope set-up is built as shown in Figure 4.8(a) with high numerical aperture (NA) objective lens that enables to collect diffraction order. Diffraction pattern from metasurface (d = 0) is measured in Fourier plane with 455, 530, and 660 nm un-polarized LEDs as light sources. Even though the wavelengths of sources are not matched with the wavelength peaking diffraction efficiency due to experimental material limitation, all of device functions according to the purpose. In Figure 4.8(c), the colors locate different ways. In order of columns, diffractions of 0^{th} blue, -1^{th} green, and 1^{th} red for RBG color splitter, -1^{th} blue, $+1^{th}$ green, and 0^{th} red for GRB color splitter, and $+1^{th}$ blue, 0^{th} green, and -1^{th} red for BGR color splitter are presented. Whole experiments are measured by color CCD (Flea 3 FL3-U3-20E4C, Point Grey Research) fixing camera setting such as exposure, shutter speed, and gain. Figure 4.8(d) displays normalized intensity distribution. Since the beam size is much larger than sample feature size, the 0^{th} diffraction is overlapped with directly propagating light without interaction by device. In addition, a little bit of noise in terms of RBG color splitter originates in wavelength of source mismatching the target wavelength.

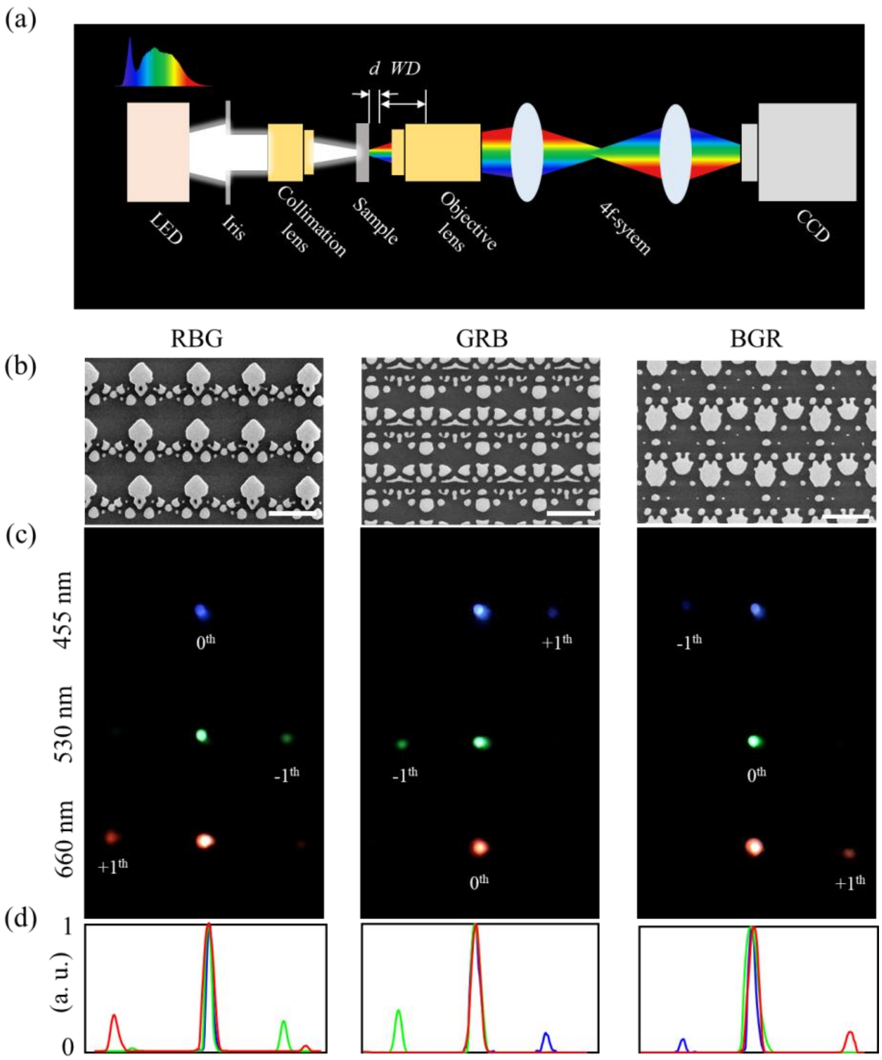

Figure 4.8 (a) Schematic diagram of experimental set-up. (b) Fabricated sample image captured by FE-SEM with 1 μm of scale bar. (c) Experimental results at Fourier plane at three wavelengths. Each column of (b-d) corresponds to an individual color splitter.

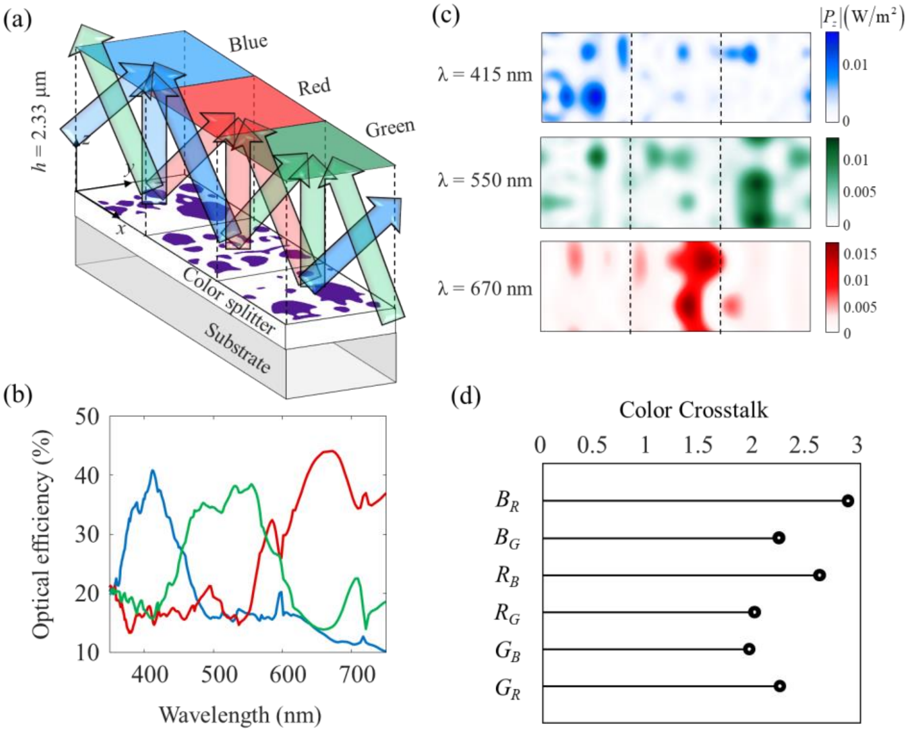

Figure 4.9 (a) Schematic illustration of the designed color splitter array in order of RBG, GRB, and BGR along *x*-direction. (b) Optical efficiency at the distance of *d* = 2.33 μm from color splitter. (c) Normal-directional Poynting vector. (d) Color crosstalk in each sub-pixel.

I turn to integration of optimized metasurface above as depicted in Figure 4.9(a). Minimizing near-field interference, they are disposed in *y*-directional offset. To measure field distribution and optical efficiency, full field simulation on FDTD is utilized. As expected, Poynting vector distribution of normal direction at the distance of 2.33 μm from the metasurface layer shows distinctly spatial color splitting in Figure 4.9(b). The dominant power distributions at peak wavelengths of 415, 550 and 670 nm are focused on left side, right side and middle, respectively in Figure

4.9(c). Optical efficiency, which is defined by integrating and normalizing power distribution at each region, reaches near 40 % or higher. Furthermore, color crosstalk is calculated by the ratio between integration of target color *i* and undesired color *j* from center wavelength $\lambda_{i,j}$ as Eq. (4.6).

$$i_j = \int_{\lambda_i - 30}^{\lambda_i + 30} T_i\left(\lambda_i\right) d\lambda_i \Big/ \int_{\lambda_j - 30}^{\lambda_j + 30} T_i\left(\lambda_j\right) d\lambda \tag{4.6}$$

Since baseline of optical transmission that causes whitening as shown in Figure 4.9(d), color crosstalk is not much higher than conventional absorptive color filters. However, it has much lower white light than previous works [28]. Thus, the proposed metasurface can be more effective device in color quality.

Equivalent device for experiment is fabricated by the same process mentioned above. Figure 4.10 shows the fabrication and experimental results for demonstration of the integrated color splitter. The fabricated sample in Figure 4.10(a) shows little deviation from the optimized pattern except small rods and rods circumventing holes. This does not affect purposed operation much. To measure performance of full-color pixel, the same experimental set-up of Figure 4.8(a) except Fourier lens is utilized. Different form far-field distribution, image plane at the distance of d =2.33 μm from metasurface is transferred. In addition, white LED (MNWHL4, Thorlabs) illuminating neutral white (4900 K) is used for full-color imaging. The measured image plane show good agreement with the purposed color distribution. Since this color depends on sensitivity of CCD camera and spectrum of white light source, it is distorted color that does not exactly same with simulation environment. Thus, color calibration of image is essential for commercial camera such as color correction, gamma correction, and white balance.

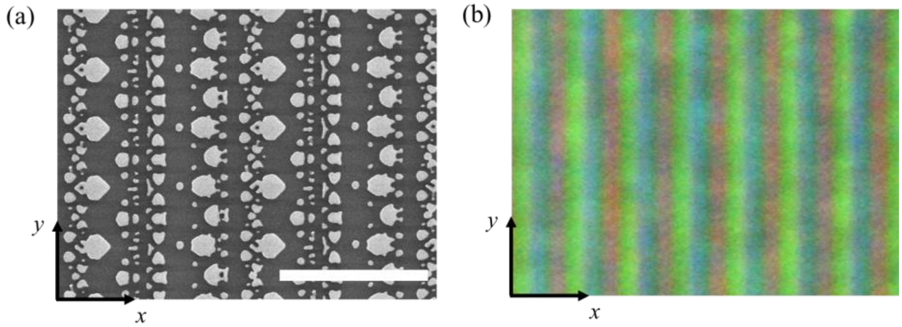

Figure 4.10 (a) FE-SEM image of integrated color splitters. The white scale bar denotes 3 μm. (b) Measured image at the distance of 2.33 μm from metasurface.

4.4 Image quality evaluation

This section discusses image quality produced by the integrated full-color splitters. From the optical efficiency as displayed in Figure 4.9(b), the detected power enhancement compared to color filters that are integrated in typical on-chip CMOS image sensor achieves about 2.073. From the multispectral color about Gretag-Macbeth color checker under the d65 light illumination, the color difference relating with color fidelity is compared. Figure 4.11 represent color checker and color degradation by metasurface. It looks not much different colors between color patches in Figures 4.11(a) and 4.11(b), while conventional dye color filters show much darker than the others as shown in Figure 4.11(d). The quantified color difference is much higher than just-noticeable difference in Figure 4.11(e) [62]. Therefore, color correction matrix (CCM) is optimized by linear interpolation that reduces color difference:

$$\mathrm{CCM} = \begin{pmatrix} 1.1589 & -0.0094 & -0.0083 \\ -0.0044 & 1.1476 & 0.0032 \\ -0.0071 & 0.0015 & 1.1244 \end{pmatrix} \tag{4.7}$$

The off-diagonal element of CCM is little that means color crosstalk is remarkably low. On the other hand, the diagonal element of CCM is about 1.1, which denotes the color difference is originated by lightness. In results, the CCM elicits that all of color difference between corrected color and Macbeth color checker is lower than 1.5 in Figure 4.11(e), which is hardly and slightly noticeable range. Thus, the color can be successfully reconstructed.

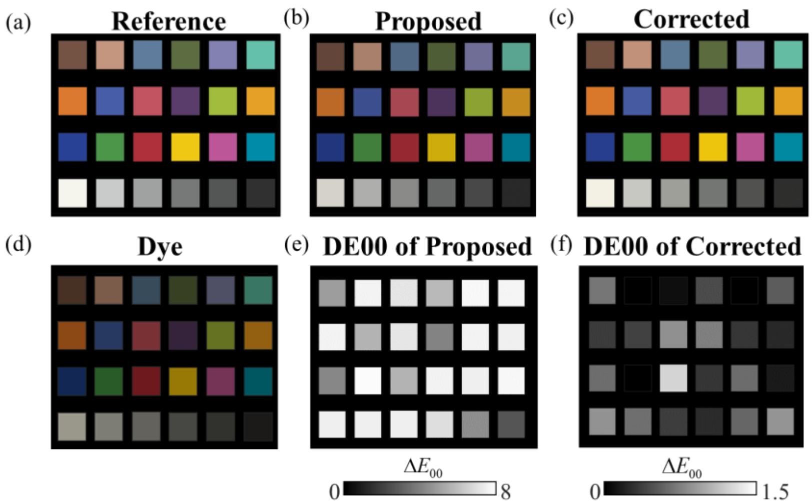

Figure 4.11 (a) Macbeth color checker to calibrate color as reference color. (b) Color checker passing through the proposed metasurface. (c) Color checker calibrating through color correction matrix. (d) Color checker passing through the conventional dye color filters. (e) Color difference 2000 between (a) and (b). (f) Color difference between (a) and (c).

Additionally, I discuss noise tolerance adding to raw image for three cases, conventional dye color filters, the proposed metasurface, and color correction. Process of calculating PSNR is as follows: prepare for target image of which color has pure red, green, and blue. This makes easy to convolve spectral response between individual pixel and spectrum of device.

For example, spectra of blue, green, and red pixel of image functions as bandpass filters (B < 500 nm, 500 nm < G < 580 nm, and R >580 nm) with perfect transmission. This means that convolution with device is multiplication between each pixel and the average of total spectra, which is transfer function of metasurface in the range of R, G, and B band. After then, white Gaussian noise is added to raw image. This Gaussian noise describe inevitable noise in image sensors such as thermal noise and dark current noise. Small sensor PSNR can be corresponds to low-light condition.

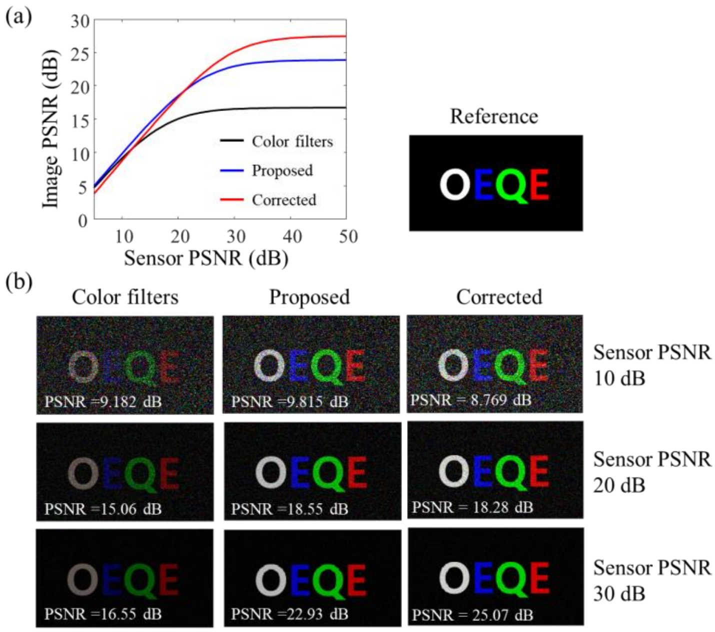

Figure 4.12 (a) Image PSNR under the additive Gaussian noise defining sensor PSNR to raw image for the conventional color filter, the proposed metasurface, and the metasurface with color correction matrix. The reference image is full color “OEQE” letters. (b) Raw image and its PSNR for 10, 20, and 30 dB of sensor PSNR.

Increasing PSNR of image sensor, raw images that passing through color filters and metasurface increases PSNR but it is limited by the physical device in front of sensor and expanded by post-processing of color correction. Figure 4.12(a) points out the proposed metasurface has much qualitative image quality rather than conventional dye color filters. In low light condition under 15 dB of sensor PSNR, they have similar PSNR, but the proposed full-color splitter outperforms higher than 15 dB. Moreover, the post-processing using color correction which is calculated in Eq. (4.7) exhibits much higher PSNR. Verifying higher PSNR provides better image quality, Figure 4.12(b) illustrates a plethora of full-color “OEQE” images. At the low light condition (Sensor PSNR = 10 dB), all image is degraded by much noise. Especially, the image from color filters shows dimmed image due to limited transmission efficiency. In contrast, the reconstructed images for metasurface displays definite image quality. Therefore, the proposed freeform full-color splitter array shows apparent advantages over SNR.

4.5 Discussion about off-axis color splitters

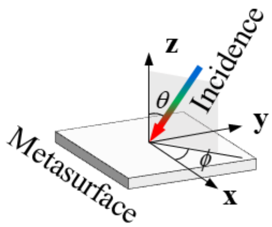

Figure 4.13 Coordinate for oblique incidence on metasurface

In practical image sensor, prime ray of incident light on image sensor has different angle depending on pixel position. It denotes that color splitters for off-axis light are required for each pixel. Thus, this section demonstrates the possibility to optimize nanostructures for off-axis light. In optimization process, the optimized nanostructures for normal incidence in previous sections are modified which are utilized as initial condition with added gradients. The angle of incidence is considered in azimuthal angle (ϕ) and slanted angle (θ) as shown in Figure 4.13. For θ = -10° and -20°, nanostructures are optimized for the splitters of GRB [Figure 4.14], RBG [Figure 4.15], and BGR [Figure 4.16]. In the case of $\theta = 0^{\circ}$, the variation of azimuthal angle denotes polarization rotation which corresponds to results of Figure 4.3. Every color splitter is deformed from the pattern of normal incidence. The patterns show *y*-symmetry for $\phi = 0^{\circ}$ and the larger azimuthal angle the more complex pattern. This is because the distribution of mode index determined by pattern is dependent on incident angle.

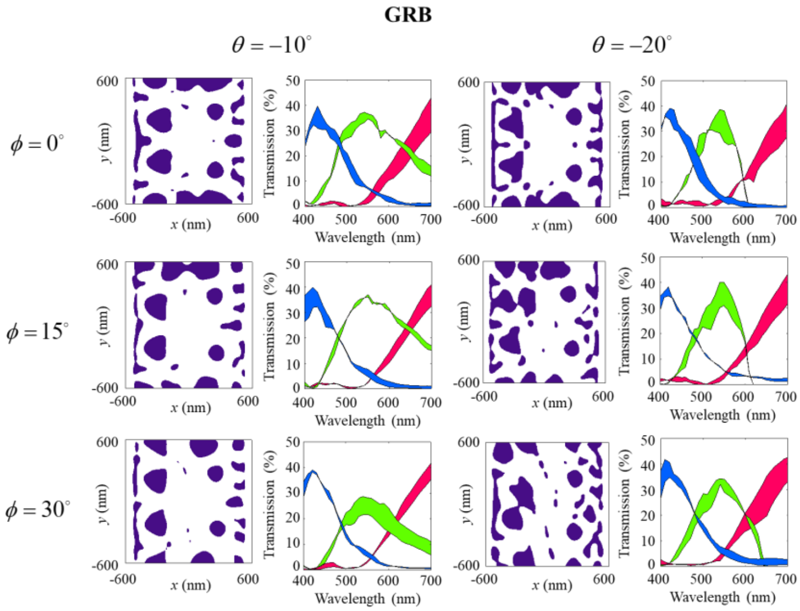

Figure 4.14 Optimized patterns of GRB color splitter and its diffraction efficiencies for $\theta = \left[-10^{\circ}, -20^{\circ}\right]$ and $\phi = \left[0^{\circ}, 15^{\circ}, 30^{\circ}\right]$.

Diffraction efficiencies for suggested angle of incidence shows robust diffraction efficiencies in Figures 4.14 and 4.16 except RBG color splitter in Figure 4.15. By Snell's law, refracted beam from incident angle of -20 degrees has transmitted angle of about 30 degrees in air. Thus, the device suffers from decreased effective thickness of complex rods along propagation axis and parallel axis giving rise to degraded modulation efficiency. For the RBG device, the diffraction efficiency of 1st order is suppressed as shown in Figure 4.15. To examine it in detail, the well-known diffraction angle is given in Eq. (4.8),

$$\theta_{\mathrm{t}} = \arcsin\left(n_{SiO_2} \sin\left(\theta_{\mathrm{in}}\right) - \frac{\lambda}{P} \right), \tag{4.8}$$

where θ_{in}, θ_{t} are incident and diffraction angle. For θ_{in} = -20°, the light above the wavelength of 600 nm cannot transmitted by total internal reflection. This is why the diffraction efficiency is very low at 1st order of RBG device. To relieve this limitation, it requires larger pixel pitch.

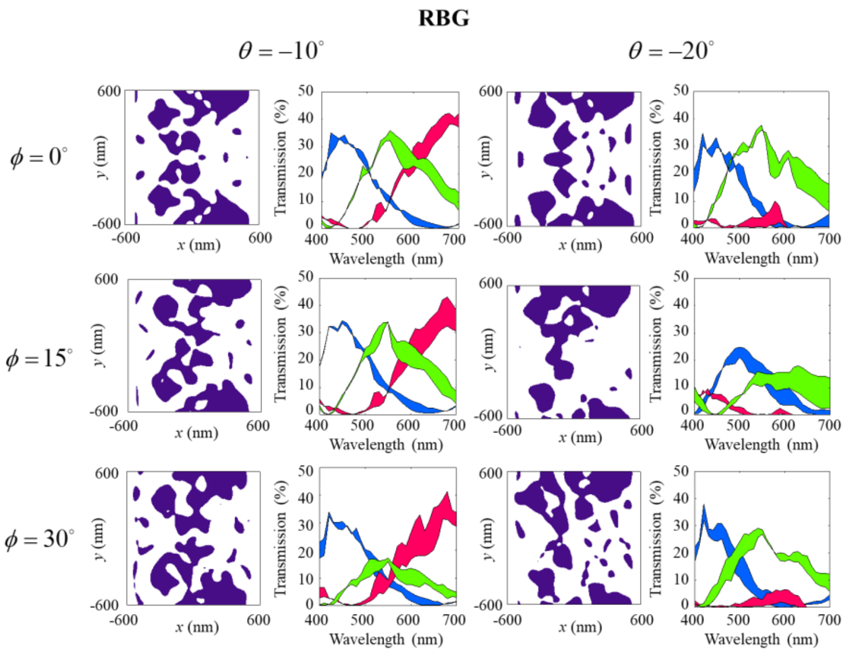

Figure 4.15 Optimized patterns of RBG color splitter and its diffraction efficiencies for $\theta = \left[-10^{\circ}, -20^{\circ}\right]$ and $\phi = \left[0^{\circ}, 15^{\circ}, 30^{\circ}\right]$.

In this regime, it should be careful of integration of color splitters because of color crosstalk in the proposed pixel pitch. Since the pixel pitch is not enough to accommodate slanted angle, angle tolerable color pixel based on color splitter array requires larger pixel pitch.

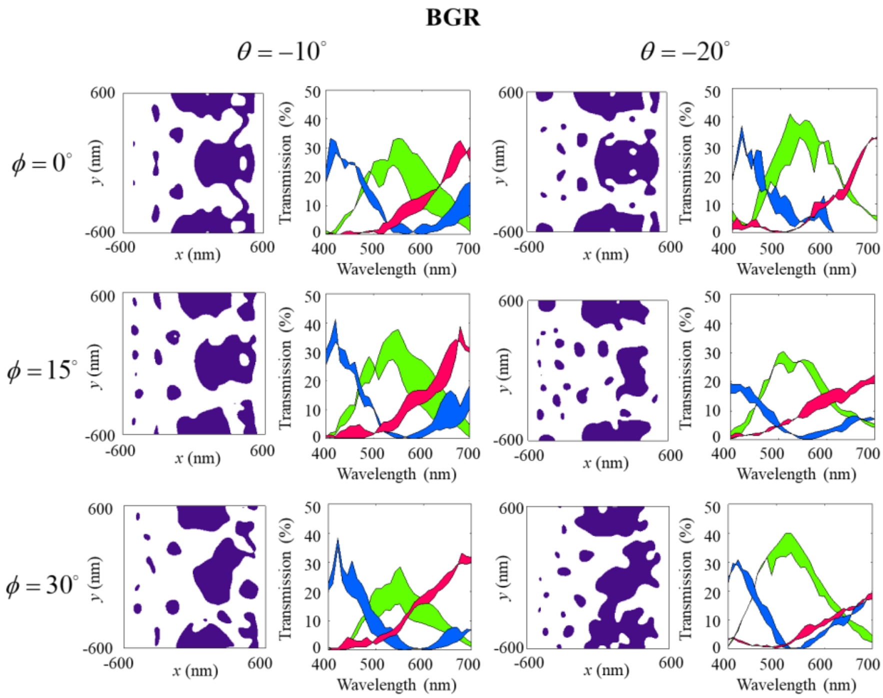

Figure 4.16 Optimized patterns of BGR color splitter and its diffraction efficiencies for $\theta = \left[-10^\circ, -20^\circ\right]$ and $\phi = \left[0^\circ, 15^\circ, 30^\circ\right]$.

The smallest rod size of total patterns has about 30 nm-diameter and its aspect ratio is 20:1 with 600 nm-thickness. In fabrication process based on e-beam lithography, it is challenge to pattern rods under 50 nm-size empirically. However, the device operates without those smallest rods because most of dominant effective modes are not confined in them as shown in Figure 4.5. Thus, the device can be implemented by the suggested e-beam lithography method.

4.6 Conclusion

This chapter has implemented full-color splitter for micron pixel image sensors. Combination of three color splitters covers every pixels replacing color filters. Each color splitter divides light along the way of diffractions orders with wavelength dependent. Previous color splitter metasurface for image sensor suffered from white light noise and impossibility to cover whole pixel due to principle of rectangular antenna. Here, the author proposed freeform metasurface that enables high diffraction efficiency inducing complex effective modes interactions. which is optimized by GPU-accelerated RCWA. The transmission efficiency leads to conventional absorptive color filters and color gamut was analyzed. Through fabrication of each color filters and integration form, desired diffraction and color distribution is experimentally measured. Even though based white line and small color cross talks exists, transmission efficiency reached 40 % which is larger than color filter limitation of 33 %. Moreover, color imaging analyzes Macbeth color checker and the proposed metasurface remains small amount of color difference. In color analysis and SNR analysis, color calibration method is utilized through color correction matrix (CCM), which increases color quality and SNR. Furthermore, the color splitters for the off-axis incident light are proposed. It is noteworthy that the proposed metasurface can boosts total image quality in terms of color quality and SNR.

Chapter 5 Plasmonic metasurface cavity for simultaneous enhancement of optical electric and magnetic fields

5.1 Introduction

Miniaturization of pixel in CIS has decreased SNR due to low numbers of photon per pixel, which makes difficulty to distinguish signal and intrinsic noise such as thermal and shot noise. Meanwhile, pixel size reduction has triggered deeper depth of photodiodes to convert light into photocurrent as much as possible, which hinder fabrication of deep-trench isolation that prevents interference among pixels. This raises an issue with regard as development of framework in thin and efficiently photon-electron converters. One substitute of deep photodiode could be a quantum dot (QD) or a perovskite integrated CIS, which can implement broadband absorption with low cost infrared (IR) photodetector and photovoltaic devices [76, 77]. As the similar way, plasmonic hot electrons, which is generated at metal-semiconductor Schottky junction, have been advanced thanks to its applicability for wavelength-tunability of plasmon-excited current [78]. In principle, both of devices are related with intensity of electromagnetic field that can be coupled with semiconductor [79]. Furthermore, it has been exhibited that electromagnetic field enhancement coupled with active region induces large photoluminescence and photocurrent [80]. Thus, strong electromagnetic intensity distribution in compact region enables pixel size reduction for infrared band and thin photodiode.

In the field of nanophotonics, harnessing light energy in nanoscale has been a significant issue with the rise of plasmonics [81, 82]. Surface plasmons (SPs) excited on the metallic surface can confine light without cut-off phenomenon when they are guided into deep subwavelength volume while dielectric nanoresonators cannot reduce their mode volume beyond diffraction limit. Many plasmonic nanofocusing applications including micro / nanoscopy [82], biosensors [83], harmonic generation enhancement[84, 85], optical tweezing [86], nano-lithography [87], and spontaneous emission control [88-90] share a common goal, which is extreme enhancement of electromagnetic energy in ultracompact volume. There have been many studies suggesting extreme electric field enhancement with various tapered metallic tips [91] or metal-insulator-metal (MIM) type resonators [92-95] resulting in about 10^4-fold enhancement of electric field intensity[96]. On the other hand, less attention has been paid on boosting nanoscale magnetic field intensity [97-100] despite various potential applications in nanophotonics and quantum optics including magnetic micro / nanoscopy [101], and magnetic Purcell effect [102]. It is generally owing to intrinsically lower power of magnetic field compared to that of electric field due to impedance relation. Moreover, it has been hard to squeeze magnetic field into a deep-subwavelength space owing to wavelength-dependence of magnetic resonance volume with circulating current unlike cases of electric field nanofocusing [103]. Hence, boosting both electric and magnetic light-matter interactions with simultaneously boosted electromagnetic fields is potentially fruitful for various fields of optics. There have been only few studies to achieve this goal with plasmonic nanoantennas containing MIM structure [104, 105]. Metallic cap-connected bow-tie nanoantenna for simultaneous enhancement of optical electric and magnetic fields proposed by Roxworthy and Toussaint [104] lacks experimental verification and feasible suggestion of simple fabrication method. Similar work by Chen *et al*. [105] also shows simultaneously boosted electric and magnetic fields with circulating plasmonic surface current. However, their work is not easy to be reproduced for large area fabrication and mass production since ion beam milling technique for thin metallic bridges is crucial but highly sensitive to unstable beam conditions. Moreover, as working principle of the device is explained in phenomenological way rather than systematic and analytical manner, it seems to involve limits when expanded and applied to more complex and multifunctional systems.

Here, I propose a novel and robust mechanism working at the near-infrared wavelengths to enhance both nanoscale electric and magnetic interactions inspired from our previous work [106]. The simple and intuitive idea is proposed for novel electric dipolar nanofocusing in nanocavities in terms of both electric and toroidal parts. It is known that rigorous model of electric dipole radiation includes two parts, electric and toroidal parts [107]. In the proposed devices, electric dipolar nanofocusing of electric and toroidal parts contributions is engineered for simultaneous nanoscale squeezing of electric and magnetic fields. Incident light is squeezed with funneled plasmonic apertures via SPs for innovative boost of electric and magnetic interactions in tiny nanocavities. With clear physical principle, systematic design rule, and simply reproducible experimental demonstration, novel resonant electric dipolar nanofocusing in large area is proposed for simultaneously squeezed electric and magnetic fields in deep subwavelength volume (~λ^3/538). The rest part of the paper is organized as a follows. At first, working principle and design rule of the device are discussed. Then, experimental evidence is suggested with measurement of far-field spectrum and near-field intensity. Throughout this chapter, I conduct numerical analysis using commercial finite element method tool (COMSOL Multiphysics 5.2) and finite difference time domain solver (Lumerical FDTD Solutions). Dielectric constants of the gold and the silicon dioxide are quoted from the work done by Palik and Malitson [40, 41].

5.2 Working principle and numerical results

5.2.1 Principle of funnel-shaped metasurface cavity

To enhance both electric and magnetic fields, I propose a funnel-shape aperture as the unit-cell for light trapping as shown in Figure 5.1(a). The funnel-shaped cavity consists of a tapered antenna region for plasmon excitation with large fill-factor and a nanocavity (NC) region for the designated location of plasmonic hotspot. The plasmon concentration on NC can be achieved when cavity mode on NC is excited about electric and magnetic fields simultaneously. Specifically, symmetric E_y and anti-symmetric H_z fields are resonantly trapped in a NC with circulating current distribution. The key idea is to locate plasmonic node of H_z field and anti-node of E_y field inside the rectangular NC simultaneously. That gives rise to electric dipole moment in y-direction and toroidal dipole moment along y-direction in NC.

(a)

(b)

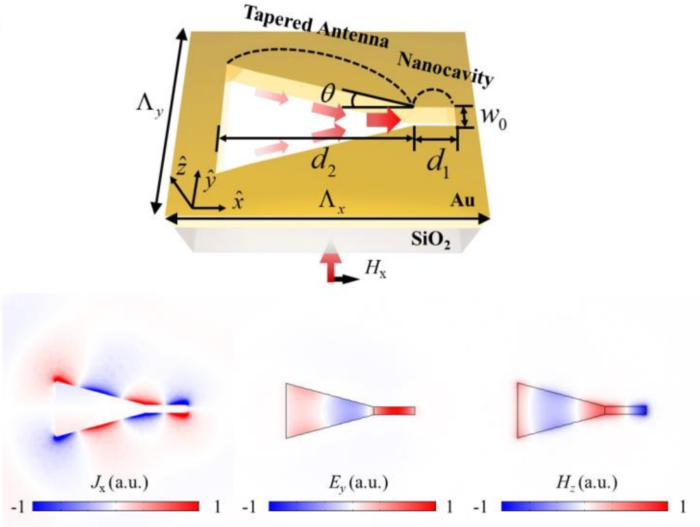

Figure 5.1 (a) A schematic of the proposed metasurface. (b) Transverse field distribution of current, electric and magnetic field.

Hence, to enhance E_y and H_z in the designated NC, I numerically optimized d_1 and d_2 parameters with w_0 and θ set to be 70 nm and 15° considering the experimental fabrication and the efficient energy trapping. It is well known that smaller plasmonic gap can be more advantageous for better field enhancement [108]. However, since resolution of our e-beam negative tone resist is limited, it is hard to guarantee precise large area patterning of NC parts without residue problem after lift-off. Hence, w_0 is fixed as 70 nm for reducing fabrication error. When I choose value of θ, there was a criterion to consider as follows. If θ is too small and tapering angle is adiabatically formed, plasmonic energy would be trapped in the unit cell funnel-shape aperture in nearly homogeneous manner so that effect of plasmonic focusing into the rectangular NC can be weakened. On the other hand, if θ is too large, SPs can be hard to funnel into the rectangular NC and most of plasmonic energy can be absorbed at tapering region rather than the NC region. Hence, I fixed θ as moderate value of 15° which is conventionally familiar value in near-field scanning optical microscopy [109, 110]

It is important to determine the lengths of the NC and tapered antenna, d_1 and d_2, since field intensity and patterns of the hotspots in the NC are critically dependent on them. Hence, the optimization of d_1 and d_2 was conducted to nanofocus a large portion of electromagnetic energy into the NC while symmetric E_y and anti-symmetric H_z are trapped, simultaneously. When y-polarized light is normally incident to the substrate side at a wavelength of 1120 nm, the electric dipolar nanofocusing is achieved under the condition of d_1 = 355 nm and d_2 = 750 nm with the desired anti-symmetric current density loop J_x, central symmetric E_y, and anti-symmetric H_z along x-axis as shown in Figure 5.1(b). By the resonant current density distribution, asymmetrically squeezed cavity mode is formed inside the aperture while E_y and H_z fields are trapped inside the NC.

Furthermore, a two-dimensional periodic array of the funnel-shaped aperture, which is named as the plasmonic metasurface cavity (PMC), to improve enhancement performance of electric and magnetic fields in large area. For single funnel-shaped cavity, large amount of input energy is scattered in near-field. Hence, I exploit constructive interference of SPs in a periodic array of the optimized funnel-shaped cavities for efficiency-improved nanofocusing of SPs into the nanocavities. The SP scattering by the single funnel-shaped cavity occurs dominantly at the gold/glass interface with a butterfly-like radiation pattern [Figures 5.2(a) and 5.2(c)] rather than a dipole-like radiation pattern at the air/gold interface [Figures 5.2(b) and 5.2(c)]. The difference between the SP radiation patterns originates from the difference of the refractive indices on the interfaces.

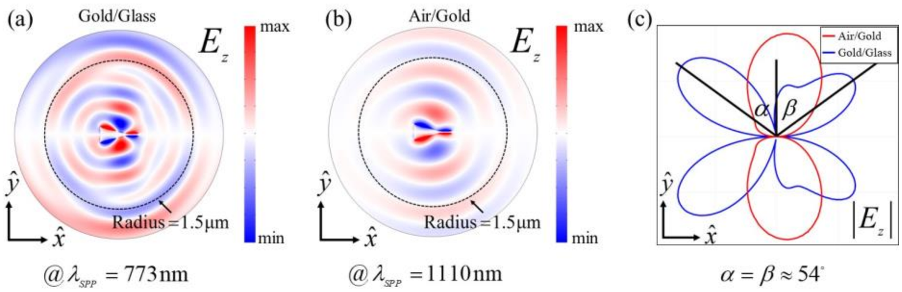

Figure 5.2 Plasmonic field distribution at the interface between (a) gold/glass and (b) air/gold with SP wavelength. (c) Radiation pattern of z-directional electric field along circle of 1.5 μm radius.

As SP wavelength at the gold/glass interface (~773 nm) is fairly shorter than that at the gold/air glass (~1110 nm), different charge distributions at the two sides of the funnel-shaped cavity cause the totally different scattering patterns, as shown in Figures 5.2(a) and 5.2(b). For the two main scattering lobes at the gold/glass interface, the SPs are directed along the angle of $\alpha = \beta \approx 54°$ [blue contour in Figure 5.2(c)]. Furthermore, the SP scattering intensity at the gold/glass interface is almost twice higher than that at the air/gold interface. Hence, I only consider the SP-assisted constructive interference at the gold/glass interface to enhance total field enhancement factors, where $\Lambda_x \approx 2\ \lambda_{sp}\ \sin\alpha \approx 1200$ nm and $\Lambda_y \approx 2\ \lambda_{sp}\ \cos\alpha \approx 890$ nm ($\lambda_{sp} =$ 773 nm at the wavelength of 1120 nm). Consequently, the enhancement factors of average electric field intensity and magnetic field intensity markedly increase by virtue of the constructive interference.

5.2.2 Discussion

There is broadband electromagnetic enhancement as described in Figure 5.3(a), which are investigated in the deep-subwavelength ($w_0 \times d_1 \times h = \lambda^3/538$) sized rectangular NCs in Figure 5.3(a). The average electric intensity reaches its highest point 45 times at 1150 nm-wavelength near the target wavelength and the average magnetic intensity reaches 11 times at 1150 nm-wavelength. This wavelength deviation originates from imperfect matching of period due to aperture. As shown in Figure 5.3(b), not only electric energy density focused on NC region but also magnetic energy density is improved at tip. This broadband optical field confinement denotes that light energy is strongly coupled with materials. For example, quantum dot emitter has broadband absorption bandwidth in near-infrared region and its Purcell factor can be boosted.

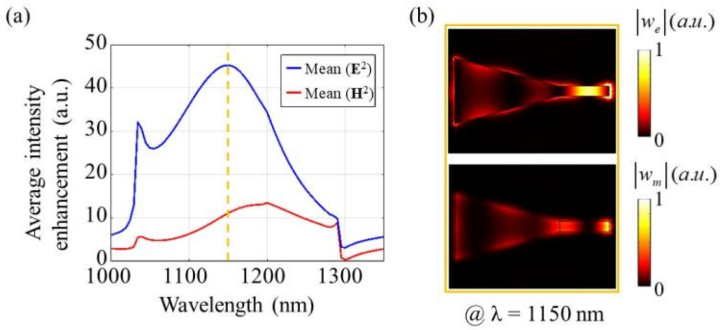

Figure 5.3 (a) Average electromagnetic intensity enhancement in NC region. (b) Electric and magnetic energy density distribution at the middle of metal film.

Before experimental demonstration of this device, it is difficult to quantify enhancement factor by near-field scanning optical microscopy because it cannot estimate average or volumetric enhancement factor. Thus, I assume that transmission is contributed by multipolar scattering that dominantly assists for field enhancement including electric, magnetic and toroidal dipoles. In comparison between multipole contribution to transmission and numerical/experimental transmission, I can infer that the light is confined and enhanced in deep-subwavelength volume. Furthermore, near-field distribution is measured by NSOM to support device verification. The multipole decomposition of electromagnetic distribution is calculated by current distribution as follows:

$$\begin{aligned}
p_\alpha &= -\frac{1}{i\omega}\int d^3\boldsymbol{r}\,\boldsymbol{J}_\alpha^\omega j_0(kr), \\
T_\alpha &= -\frac{k^2}{2i\omega}\int d^3\boldsymbol{r}\left[3(\boldsymbol{r}\cdot\boldsymbol{J}_\omega)r_\alpha - r^2\boldsymbol{J}_\alpha^\omega\right]\frac{j_2(kr)}{(kr)^2}, \\
m_\alpha &= \frac{3}{2}\int d^3\boldsymbol{r}\left(\boldsymbol{r}\times\boldsymbol{J}_\omega\right)_\alpha \frac{j_1(kr)}{kr}\ (\alpha = x, y, z),
\end{aligned} \tag{5.1}$$

where $\boldsymbol{J}$, $\boldsymbol{r}$, k, and j_n denote electric current density, position vector, wave number, and the first kind spherical Bessel function [111]. Contributions of electric and magnetic quadrupoles are excluded as the values are extremely low compared to other dominant terms in Eq. 5.2.

$$\begin{aligned}
C_{sca}^{total} &= C_{sca}^{p} + C_{sca}^{m} + C_{sca}^{Q^e} + C_{sca}^{Q^m} = \frac{k^4}{6\pi\varepsilon_0^2|E_{inc}|^2}\left[\sum_\alpha\left(|p_\alpha|^2 + \frac{|m_\alpha|^2}{c^2}\right)\right. \\
&\left. + \frac{1}{120}\sum_{\alpha\beta}\left(|kQ_{\alpha\beta}|^2 + \left|\frac{kQ_{\alpha\beta}}{c}\right|^2\right) + \cdots\right],\ (\alpha = x, y, z)
\end{aligned} \tag{5.2}$$

By decomposing field distribution into multipole family at NC region only, the scattering cross-section that contributes to transmission is calculated and shown in Figure 5.4. The summation electric and toroidal dipole moment terms, which is called C^{p}_{sca} is much higher than other terms. This is because the electric and toroidal dipoles along *y*-direction are induced by dominant enhanced-field, while dominant magnetic dipole directs the surface-normal. Thus, the induced magnetic dipole little contribute transmission.

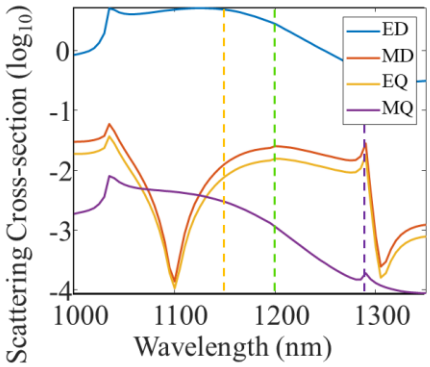

Figure 5.4 Scattering cross-section from decomposed multipoles

5.3 Experimental results

To implement the proposed metasurface, it is fabricated by e-beam lithography and lift-off process as shown in Figure 5.5. The detailed fabrication recipe is as follows. The fabrication process starts on a 500 μm-thick fused silica substrate. The structures were defined in the negative tone resist (ALLRESIST, AR-N 7520.18) by standard electron-beam lithography (ELIONIX ELS-7800, 80 kV, and 50 pA). The resist layer was spin-coated (5000 rpm, 60 seconds) and baked at 80 °C on the hotplate for 50 seconds and its final thickness was about 500 nm. In order to prevent charging effect from the dielectric substrate, a conductive polymer layer (Showa Denko, E-spacer 300Z) was spin-coated (2000 rpm, 60 seconds) before electron-beam exposure step. Electron beam exposure dose was around 1200~1300 μC/cm^2.

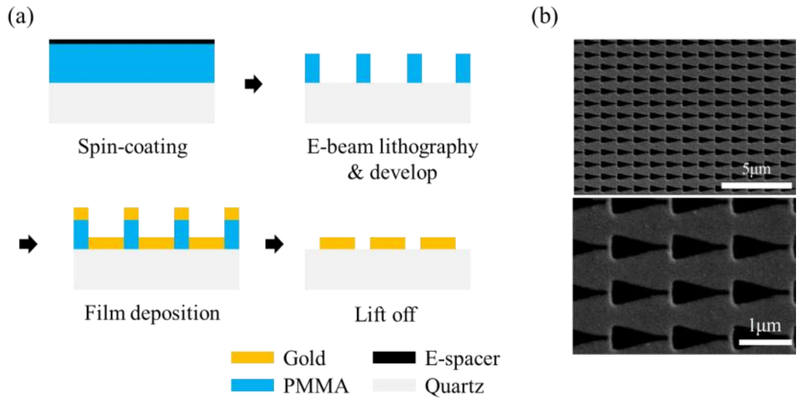

Figure 5.5 (a) Fabrication process of the proposed metasurface (b) SEM image of fabricated metasurface

After exposing, a conductive polymer layer was removed in the DI water for 90 seconds. Then, AR-N resist was developed in the AR-300 47 solutions (ALLRESIST) for 50 seconds and rinsed by DI water for 60 seconds. After that, post-bake process was done at 85 °C on the hotplate for 60 seconds. After post bake process, Cr (3 nm) and Au (100 nm) were deposited by electron-beam evaporation (KVT KVE-ENS4004), followed by lift-off process in 50 °C hot-acetone. Sample image is captured by scanning electron microscope (HITACHI S-4800) as shown in Figure 5.5(b). It looks similar with the designed metasurface, while the abrupt angle at NC has deviation.

To measure transmission spectra, microscopic spectrum analyzer is set up as described in Figure 5.6(a). The super-continuum light source (NKT Photonics, Super EXTREME EXR 15) is used for a broadband source. Due to smaller sample size than source, plano-convex lens is used. To find and illuminate on the metasurface correctly, imaging setup is utilized through 50:50 beam splitter. And then the transmitted signal is collected through an optical fiber and measured by optical spectrum analyzer (ANDO, AQ6317B). In Figure 5.6(b), the numerically calculated transmission spectrum and experimental spectrum are compared. Since the 50:50 beam splitter is inserted on transmission, it is reasonable to take double the experimental spectrum. The measured transmission is near the measured transmission spectrum through the sample shows the strong similar peak at the wavelength of 1120 nm near the maximum enhancement wavelength and it matches well with the peak that appears in the numerically calculated transmission spectrum. The measured transmission spectrum comes with spectral broadening and red-shift. I guess the imperfect fabrication of deep-subwavelength NC region could result in those effects.

In addition to far-field spectrum, near-field distribution is measured by near-field scanning microscopy (NSOM). As depicted in Figure 5.7(a), broadband source with bandpass filter functions as single wavelength source near the designed wavelength. The near-field is collected by NSOM tip and amplified by avalanche photo-detector. The bright region in Figure 5.7(b) can be corresponded with computational electric field distribution on NC region in Figure 5.7(c). As mentioned above, it is impossible to relative enhancement factor inside gap. Thus, transmission spectra and near-field distribution could be proof of the operation of the proposed metasurface.

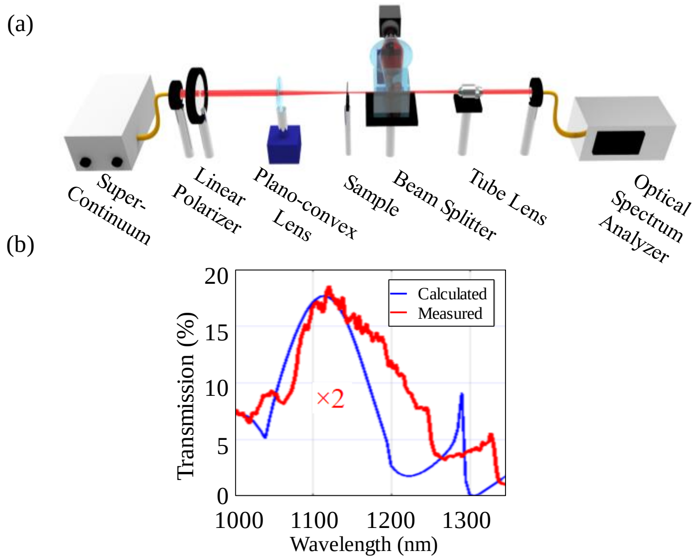

Figure 5.6 (a) Schematic illustration of the custom-built spectroscopy. (b) Normalized transmission spectra by FEM calculation and experimental measurement.

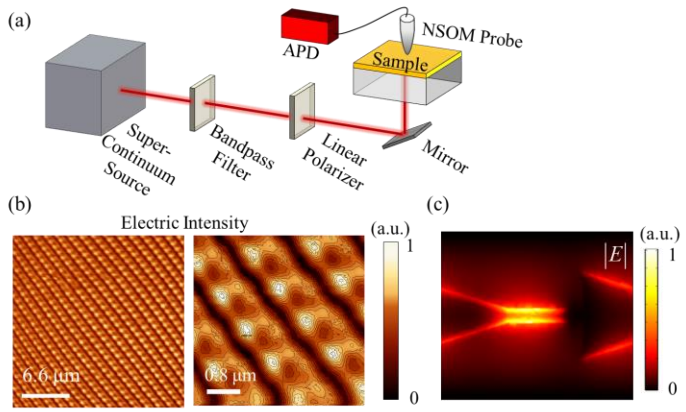

Figure 5.7 (a) Schematic illustration of the custom-built NSOM. (b) Measured electric field and simulation result on the surface on metasurface.

5.4 Purcell effect

To verify the proposed metasurface affects enhancement of light-matter interactions, analysis on Purcell effect with increasing radiative decay rates is presented. In FDTD simulation, dipole sources are located at the maximum electric or magnetic fields under plane wave illumination. The dipole source simulation assumes that the dipole source perfectly couples with total electric field **E**(r_0) and magnetic density field **B**(r_0) from metasurface as described in Eq. (5.3):

$$\begin{aligned} F_p^e &= \frac{\omega_0}{2}\mathrm{Im}\left[\mathbf{d}^* \cdot \mathbf{E}\left(r_0\right)\right], \\ F_p^m &= \frac{\omega_0}{2}\mathrm{Im}\left[\mathbf{m}^* \cdot \mathbf{B}\left(r_0\right)\right], \end{aligned} \tag{5.3}$$

where F_p^e, F_p^m, **d** and **m** indicate electric Purcell factor, magnetic Purcell factor, electric dipole moment and magnetic dipole moment, respectively. The total field consists of incident field and scattered field by inhomogeneous environment that induced by dipole sources. Furthermore, Purcell factor is sum of radiative decay rate and non-radiative decay rate,

$$F_p = \gamma_{rad} + \gamma_{non-rad}. \tag{5.4}$$

In FDTD simulation, radiative decay rate indicates the ratio between radiative decay rate from dipole without metasurface and one with metasurface per dominantly excited polarization, which are E_y, H_x, and H_z dipoles. Figure 5.8 gives the radiative decay rates excited by E_y and H_z dipoles are alike electric and magnetic field enhancement, where the interaction with material is excited by both of electric and magnetic field ways. In addition, it resembles with transmission efficiency for plane wave incidence. Thus, the tendency of Purcell factor represents the analysis above in section 5.2 and 5.3, where the proposed metasurface enhances light-matter interaction through deep subwavelength field confinement.

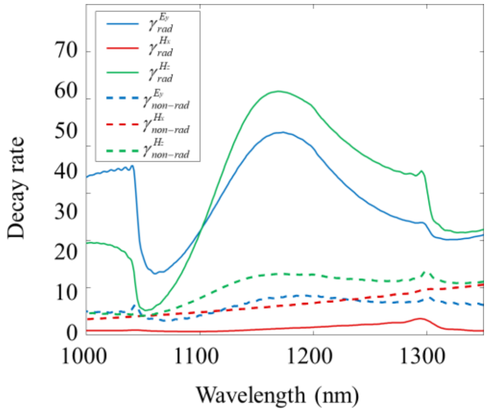

Figure 5.8 Radiative and non-radiative decay rates calculated by dipole source. The solid lines and dashed lines denote radiative and non-radiative decay rate, respectively.

5.5 Conclusion

In this chapter, a concept of plasmonic field enhancement that may overcome low SNR and photodiode thickness is treated, which can be applied to infrared image sensor. The funnel-shaped aperture array on gold nanofilm gives rise to plasmonic resonance and constructive interference of SPP. The squeezed light into cavity of $\sim\lambda^3/538$ induces enhanced density of both electric and magnetic fields. The performance of the proposed design is numerically and experimentally analyzed. This result can be integrated with quantum dot in boosting multipolar contribution in semiconductor. Moreover, polarization dependent operation of device can be applied to optically switchable device. This would be fruitful for other nanoscale light-matter interacting device such as near-field spectroscopy or bio-molecular sensing.

Chapter 6 Conclusion

In this dissertation, nanophotonic elements for CMOS image sensors in order to push the limitations of image sensors have been discussed. Beginning with light interaction with underlying materials, principles of nanostructures consisting of metasurfaces are given. Plasmonic metasurfaces can be used for deep subwavelength scale, while dielectric metasurface enable high efficient devices. Meanwhile, hyperbolic material consisting of both materials functions as anisotropic material and facilitates band manipulation. This dissertation is based on those material platforms that proceed to color filter, color pixel, and field enhancement.

In Chapter 3, a metasurface color filter is designed and analyzed that suppresses reflection by selective broadband absorption of tapered hyperbolic metamaterials. Consecutive plasmonic resonances depending on varying fill factor and size regardless of polarization state are inversely designed by particle swarm optimization method. Sub-micron color filter is demonstrated whose sub-pixel pitch is 255 nm in Bayer pattern. Optimized device achieves in reflection under 8 % as well as transmission above 35 % in visible wavelength. As the aspect of color science, oblique incident angle on each color pixel allows ±10 degrees for TM polarization and ±15 degrees for TE polarization. This device can contribute to replacing color filters of ultra-thin and small pixel, where the reflection is one of obstacles in image sensor because internal reflection in camera is a factor of image quality degradation.

In Chapter 4, full-color metasurface color pixel is examined that integrates three metasurface color splitters dividing light into (1, 0, -1) orders for combination of R, G, and B colors. Three metasurface color splitters are individually optimized by gradient-based inverse design providing freeform shape of meta-atoms. Each of them reaches near 40 % of diffraction efficiency independent of polarization state, which outperforms conventional color filter. Carefully disposing three color splitters, full-color color pixel is also implemented, which focuses light by directing relevant color pixel. Experimental results support the proposed metasurface. Moreover, outperformed color reconstruction quality and SNR show apparent advantages over dye color filters. Hence, the proposed metasurface color pixel may lead to conventional color filter arrays and be substitution in image sensor system.

In Chapter 5, novel shape of plasmonic aperture is suggested that may enhance light-matter interactions in photodiode layer. It shapes funnel consisting of tapered slit and rectangular nanocavity at the tip. Plasmon resonance along periphery induces field confinement into nanocavity region of which size is $\sim \lambda^3/536$. Symmetric electric and anti-symmetric magnetic field in nanocavity achieves 45 times and 11 times of average enhancement, respectively. Multipolar decomposition shows that dominant enhancement field is consistent with dominant scattering cross-section. Here, experimental implementation provides agreement with simulation result in far-field transmission and near-field distribution. By the same token, it is related with light-matter interaction enhancement termed as Purcell effect. Arranging electric and magnetic dipoles along dominant field component, scattered light by environment enhances decay rate from dipoles. Hence, this device shows glimpse into near-infrared camera and contributes to small geometric shaped photodiodes, which allows operation in low light amount.

Throughout dissertation, it is noteworthy that the proposed metasurfaces suggest possibility to replace limited optical system with metasurface ones in miniaturizing pixel size. Future image sensor requires high resolution, low light detection, and high image quality. Because it must be concomitant with signal-to-noise problem or color interference. Hence, I hope that this dissertation is cornerstone of future metasurface image sensor.

Appendix

A.1 Colorimetry

In chapter 3 and 4, metasurface color filter for image sensor will be discussed. This section mentions colorimetry and color difference. Since the development of CIE 1931, optical spectrum of scattered light and human perception have been connected corresponding to tristimulus values, $\bar{y}$, and $\bar{z}$ from the observed data as shown in Figure A.1(a) [60]. Furthermore, standard illuminant, which is theoretical visible light source, was provided in representing daylight, incandescent light, or sunlight. In this paper, I use illuminant D65 to quantify color perception as shown in Figure A.1(b).

Identifying colors, integral of multiplication among tristimulus values, spectrum from object, and illuminant spectrum is calculated:

$$\begin{aligned}
X &= \frac{100}{N}\int_{380}^{780} S(\lambda)I(\lambda)\bar{x}(\lambda)d\lambda, \\
Y &= \frac{100}{N}\int_{380}^{780} S(\lambda)I(\lambda)\bar{y}(\lambda)d\lambda, \\
Z &= \frac{100}{N}\int_{380}^{780} S(\lambda)I(\lambda)\bar{z}(\lambda)d\lambda, \\
N &= \int_{380}^{780} I(\lambda)\bar{y}(\lambda)d\lambda,
\end{aligned} \tag{A.1}$$

where $100/N$ is normalizing constant, S and I are transmission/reflection spectra and illuminant D65 source spectrum, respectively. While CIE 1931 space considers only chromaticity and assumes linear human color perception, CIELAB space expresses lightness (L^*) and non-linear response of human eye. In addition, the a^* and b^* denote chromaticity. To quantify color perception in CIELAB coordinate, CIEXYZ is used [59]:

$$
\begin{aligned}
&L^* = 116 f\left(Y/Y_n\right) - 16, \\
&a^* = 500\left(f\left(X/X_n\right) - f\left(Y/Y_n\right)\right), \\
&b^* = 200\left(f\left(Y/Y_n\right) - f\left(Z/Z_n\right)\right), \\
&X_n = 95.0489,\ Y_n = 100,\ Z_n = 108.8840, \\
&f\left(t\right) = \begin{cases} \sqrt[3]{t} & \text{if } t > \delta^3 \\ t/3\delta^3 + 4/29 & \text{otherwise} \end{cases},\ \delta = 6/29,
\end{aligned} \tag{A.2}
$$

where the normalized values X_n, Y_n, and Z_n are determined by illuminant. From Eqs. (A.1) and (A.2), the colors from scattered light are expected.

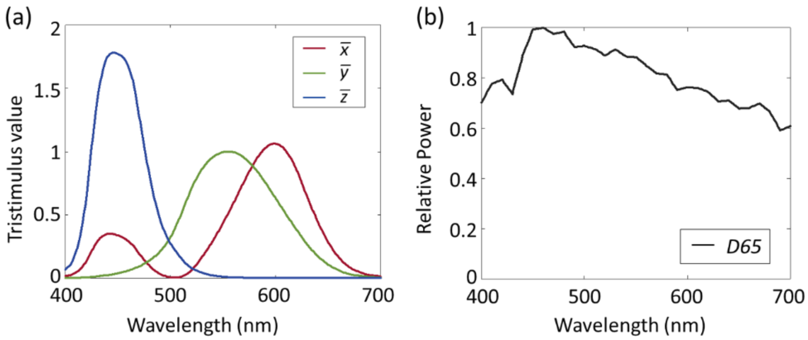

Figure A.1 (a) Tristimulus values of the CIE 1931 standard colorimetric observer. (b) Relative power spectrum of standard illuminant D65.

A.2 Color difference CIEDE2000

Color difference is a metric that quantifies how human perceives color difference noticeably. In general, the color difference has been defined as Euclidean distance in the presented coordinate such as CIERGB and CIELAB. However, there exists a non-uniformity of Euclidean color difference in CIELAB space in terms of colors due to human perceptive non-uniformities. Therefore, CIEDE2000 introduced several weighting factors and correction factors in regard to lightness, chroma, and hue in order to compare uniform difference among colors:

$$\Delta E_{00} = \sqrt{\left(\frac{\Delta L'}{k_L S_L}\right)^2 + \left(\frac{\Delta C'}{k_C S_C}\right)^2 + \left(\frac{\Delta H'}{k_H S_H}\right)^2 + R_T\left(\frac{\Delta C'}{k_C S_C}\right)\left(\frac{\Delta H'}{k_H S_H}\right)}, \quad \text{(A.3)}$$

where k_L, k_C, and k_H values are compensation terms regarding experimental condition, which are neutrally unity. In Eq. (A.3), the compensation terms for lightness, chroma, and hue are S_L, S_C, and S_H, respectively. Furthermore, the human color perception is corrected by R_T. The details of calculation procedures of compensation terms are given in ref. [61].

B. Related work

Portions of the work discussed in this dissertation are also presented in the following publications:

[Chapter 3] J. Hong, H. Son, C. Kim, S.-E. Mun, J. Sung, and B. Lee, "Absorptive metasurface color filters based on hyperbolic metamaterials for a CMOS image sensor," Optics Express, vol. 29, no. 3, pp. 3643-3658, 2021.

[Chapter 5] J. Hong, S.-J. Kim, I. Kim, H. Yun, S.-E. Mun, J. Rho, and B. Lee, “Plasmonic metasurface cavity for simultaneous enhancement of optical electric and magnetic fields in deep subwavelength volume,” Optics Express, vol. 26, no. 10, pp. 13340-13348, 2018.

Bibliography

1. M. Bigas, E. Cabruja, J. Forest, and J. Salvi, "Review of CMOS image sensors," Microelectronics Journal **37**, 433-451 (2006).

2. J. Alakarhu, "Image Sensors and Image Quality in Mobile Phones " in *International Image Sensor Workshop*(Ogunquit, 2007).

3. E. Samei, N. T. Ranger, J. T. Dobbins, and Y. Chen, "Intercomparison of methods for image quality characterization. I. Modulation transfer function," Med Phys **33**, 1454-1465 (2006).

4. G. Agranov, V. Berezin, and R. H. Tsai, "Crosstalk and microlens study in a color CMOS image sensor," IEEE Transactions on Electron Devices **50**, 4-11 (2003).

5. W. N. Ye, and Y. Xiong, "Review of silicon photonics: history and recent advances," Journal of Modern Optics **60**, 1299-1320 (2013).

6. H. J. Jang, J. Y. Lee, J. Kwak, D. Lee, J.-H. Park, B. Lee, and Y. Y. Noh, "Progress of display performances: AR, VR, QLED, OLED, and TFT," Journal of Information Display **20**, 1-8 (2019).

7. E.-S. Eid, "Study of limitations on pixel size of very high resolution image sensors," in *Proceedings of the Eighteenth NRSC'2001 (IEEE Cat. No.01EX462)*(Mansoura, Egypt, 2001), pp. 15–28.

8. C.-R. M. J. Ahn, B. Kim, K. Lee, Y. Kim, M. Lim, W. Lee, H. Park, K. Moon, J. Yoo, "Advanced image sensor technology for pixel scaling down toward 1.0 µm," in *IEEE International Electron Devices Meeting (IEDM)*(IEEE2008), pp. 1-4.

9. J. Ahn, K. Lee, Y. Kim, H. Jeong, B. Kim, H. Kim, J. Park, T. Jung, W. Park, T. Lee, E. Park, S. Choi, G. Choi, H. Park, Y. Choi, S. Lee, Y. Kim, Y. J. Jung, D. Park, S. Nah, Y. Oh, M. Kim, Y. Lee, Y. Chung, I. Hisanori, J. Im, D. K. Lee, B. Yim, G. Lee, H. Kown, S. Choi, J. L. D. Jang, Y. Kim, T. Kim, G. Hiroshige, C. C. D. Lee, and G. Han, "A 1/4-inch 8Mpixel CMOS Image Sensor with 3D Backside-illuminated 1.12um pixel with front-side

deep-trench isolation and vertical transfer gate," in *Proceedings on IEEE International Solid-State Circuits Conference Digest of Technical Papers*(IEEE2014), pp. 124–125.

10. Y. Kim, W. Choi, D. Park, H. Jeoung, B. Kim, Y. Oh, S. Oh, B. Park, E. Kim, Y. Lee, T. Jung, Y. Kim, S. Yoon, S. Hong, J. Lee, S. Jung, C.-R. Moon, Y. Park, D. Lee, and D. Chang, "A 1/2.8-inch 24Mpixel CMOS image sensor with 0.9µm unit pixels separated by full-depth deep-trench isolation," in *2018 IEEE International Solid - State Circuits Conference - (ISSCC)*(2018), pp. 84-86.

11. H. Kim, J. Park, I. Joe, D. K. J. H. Kim, D. Cho, T. Lee, C. L. H. Park, S. Hong, C. C. J. Kim, H. Lim, Y. Oh, Y. K. S. Nah, S. Jung, J. Lee, J. A. H. Hong, K. Lee, and H.-K. Kang, "A 1/2.65in 44Mpixel CMOS image sensor with 0.7 µm pixels fabricated in advanced full-depth deep-trench isolation technology," in *International Solid- State Circuits Conference - (ISSCC)*(IEEE2020), pp. 104–106.

12. D. Park, S.-W. Lee, J. Han, D. Jang, H. Kwon, S. Cha, M. K. H. Lee, S. S. W. J. Y. Lee, S. N. H. Jeong, B. K. S. Jung, J. Lee, Y. K. C.-R. Moon, and Y. Park, "A 0.8 µm smart dual conversion gain pixel for 64 Megapixels CMOS image sensor with 12k e- full-well capacitance and low dark noise," in *2019 IEEE International Electron Devices Meeting (IEDM)*(2019), pp. 16.12.11–16.12.14.

13. H. T. Chen, A. J. Taylor, and N. Yu, "A review of metasurfaces: physics and applications," Rep Prog Phys **79**, 076401 (2016).

14. G. Y. Lee, J. Sung, and B. Lee, "Metasurface optics for imaging applications," Mrs Bull **45**, 202-209 (2020).

15. J. Sung, G. V. Lee, and B. Lee, "Progresses in the practical metasurface for holography and lens," Nanophotonics-Berlin **8**, 1701-1718 (2019).

16. A. Shaukat, F. Noble, and K. M. Arif, "Nanostructured Color Filters: A Review of Recent Developments," Nanomaterials (Basel) **10**

(2020).
17. S. M. Kamali, E. Arbabi, A. Arbabi, and A. Faraon, "A review of dielectric optical metasurfaces for wavefront control," Nanophotonics-Berlin **7**, 1041-1068 (2018).
18. F. Gildas, and Y. P. Dan, "Review of nanostructure color filters," J Nanophotonics **13** (2019).
19. B. H. Chen, P. C. Wu, V. C. Su, Y. C. Lai, C. H. Chu, I. C. Lee, J. W. Chen, Y. H. Chen, Y. C. Lan, C. H. Kuan, and D. P. Tsai, "GaN Metalens for Pixel-Level Full-Color Routing at Visible Light," Nano Letters **17**, 6345-6352 (2017).
20. Z. Lin, V. Liu, R. Pestourie, and S. G. Johnson, "Topology optimization of freeform large-area metasurfaces," Opt Express **27**, 15765-15775 (2019).
21. S. Nishiwaki, T. Nakamura, M. Hiramoto, T. Fujii, and M.-a. Suzuki, "Efficient colour splitters for high-pixel-density image sensors," Nature Photonics **7**, 240-246 (2013).
22. M. Mansouree, H. Kwon, E. Arbabi, A. McClung, A. Faraon, and A. Arbabi, "Multifunctional 2.5D metastructures enabled by adjoint optimization," Optica **7**, 77-84 (2020).
23. A. Vaskin, R. Kolkowski, A. F. Koenderink, and I. Staude, "Light-emitting metasurfaces," Nanophotonics **8**, 1151-1198 (2019).
24. A. K. Azad, W. J. M. Kort-Kamp, M. Sykora, N. R. Weisse-Bernstein, T. S. Luk, A. J. Taylor, D. A. R. Dalvit, and H.-T. Chen, "Metasurface Broadband Solar Absorber," Scientific Reports **6**, 20347 (2016).
25. J. Hong, C. Kim, S.-E. Mun, J. Sung, B. Lee, "Absorptive metasurface color filter based on hyperbolic metamaterial for CMOS image sensor," Opt Express **29**, 3643-3658.
26. N. Zhao, P. B. Catrysse, and S. Fan, "Perfect RGB-IR Color Routers for Sub-Wavelength Size CMOS Image Sensor Pixels," Advanced Photonics Research **2**, 2000048 (2021).

27. P. Camayd-Muñoz, C. Ballew, G. Roberts, and A. Faraon, "Multifunctional volumetric meta-optics for color and polarization image sensors," Optica **7** (2020).

28. M. Miyata, M. Nakajima, and T. Hashimoto, "High-Sensitivity Color Imaging Using Pixel-Scale Color Splitters Based on Dielectric Metasurfaces," ACS Photonics **6**, 1442-1450 (2019).

29. J. Hong, S. J. Kim, I. Kim, H. Yun, S. E. Mun, J. Rho, and B. Lee, "Plasmonic metasurface cavity for simultaneous enhancement of optical electric and magnetic fields in deep subwavelength volume," Opt Express **26**, 13340-13348 (2018).

30. W. L. Barnes, A. Dereux, and T. W. Ebbesen, "Surface plasmon subwavelength optics," Nature **424**, 824-830 (2003).

31. Y. C. Jun, K. C. Y. Huang, and M. L. Brongersma, "Plasmonic beaming and active control over fluorescent emission," Nature Communications **2**, 283 (2011).

32. S. Y. Lee, K. Kim, S. J. Kim, H. Park, K. Y. Kim, and B. Lee, "Plasmonic meta-slit: shaping and controlling near-field focus," Optica **2**, 6-13 (2015).

33. E. Y. Song, S. Y. Lee, J. Hong, K. Lee, Y. Lee, G. Y. Lee, H. Kim, and B. Lee, "A double-lined metasurface for plasmonic complex-field generation," Laser Photonics Rev **10**, 299-306 (2016).

34. A. Arbabi, Y. Horie, M. Bagheri, and A. Faraon, "Dielectric metasurfaces for complete control of phase and polarization with subwavelength spatial resolution and high transmission," Nature Nanotechnology **10**, 937-943 (2015).

35. M. Khorasaninejad, A. Y. Zhu, C. Roques-Carmes, W. T. Chen, J. Oh, I. Mishra, R. C. Devlin, and F. Capasso, "Polarization-Insensitive Metalenses at Visible Wavelengths," Nano Letters **16**, 7229-7234 (2016).

36. S. E. Mun, C. Choi, J. Hong, and B. Lee, "Broadband wavelength demultiplexer using Fano-resonant metasurface," Nanophotonics-Berlin **9**,

1015-1022 (2020).
37. W. Liu, and Y. S. Kivshar, "Generalized Kerker effects in nanophotonics and meta-optics [Invited]," Opt Express **26**, 13085-13105 (2018).
38. A. Poddubny, I. Iorsh, P. Belov, and Y. Kivshar, "Hyperbolic metamaterials," Nature Photonics **7**, 948-957 (2013).
39. Z. Guo, H. Jiang, and H. Chen, "Hyperbolic metamaterials: From dispersion manipulation to applications," Journal of Applied Physics **127** (2020).
40. E. D. Palik, *Handbook of Optical Constants of Solids* (1998).
41. I. H. Malitson, "Interspecimen comparison of the refractive index of fused silica," J. Opt. Soc. Am **55**, 1205–1208 (1965).
42. J. Rho, Z. Ye, Y. Xiong, X. Yin, Z. Liu, H. Choi, G. Bartal, and X. Zhang, "Spherical hyperlens for two-dimensional sub-diffractional imaging at visible frequencies," Nature Communications **1**, 143 (2010).
43. A. P. Slobozhanyuk, P. Ginzburg, D. A. Powell, I. Iorsh, A. S. Shalin, P. Segovia, A. V. Krasavin, G. A. Wurtz, V. A. Podolskiy, P. A. Belov, and A. V. Zayats, "Purcell effect in hyperbolic metamaterial resonators," Physical Review B **92** (2015).
44. X. Yang, J. Yao, J. Rho, X. Yin, and X. Zhang, "Experimental realization of three-dimensional indefinite cavities at the nanoscale with anomalous scaling laws," Nature Photonics **6**, 450-454 (2012).
45. W. Yang, S. Xiao, Q. Song, Y. Liu, Y. Wu, S. Wang, J. Yu, J. Han, and D. P. Tsai, "All-dielectric metasurface for high-performance structural color," Nat Commun **11**, 1864 (2020).
46. J. H. Yang, V. E. Babicheva, M. W. Yu, T. C. Lu, T. R. Lin, and K. P. Chen, "Structural Colors Enabled by Lattice Resonance on Silicon Nitride Metasurfaces," ACS Nano **14**, 5678-5685 (2020).
47. H. Yun, S. Y. Lee, K. Hong, J. Yeom, and B. Lee, "Plasmonic cavity-apertures as dynamic pixels for the simultaneous control of colour and

intensity," Nat Commun **6**, 7133 (2015).
48. S. Bang, S. So, and J. Rho, "Realization of broadband negative refraction in visible range using vertically stacked hyperbolic metamaterials," Sci Rep **9**, 14093 (2019).
49. A. Miyamichi, A. Ono, H. Kamehama, K. Kagawa, K. Yasutomi, and S. Kawahito, "Multi-band plasmonic color filters for visible-to-near-infrared image sensors," Opt Express **26**, 25178-25187 (2018).
50. Y. D. Shah, P. W. R. Connolly, J. P. Grant, D. Hao, C. Accarino, X. Ren, M. Kenney, V. Annese, K. G. Rew, Z. M. Greener, Y. Altmann, D. Faccio, G. S. Buller, and D. R. S. Cumming, "Ultralow-light-level color image reconstruction using high-efficiency plasmonic metasurface mosaic filters," Optica **7** (2020).
51. C. S. Park, V. R. Shrestha, W. Yue, S. Gao, S. S. Lee, E. S. Kim, and D. Y. Choi, "Structural Color Filters Enabled by a Dielectric Metasurface Incorporating Hydrogenated Amorphous Silicon Nanodisks," Sci Rep **7**, 2556 (2017).
52. J. Berzinš, S. Fasold, T. Pertsch, S. M. B. Bäumer, and F. Setzpfandt, "Submicrometer Nanostructure-Based RGB Filters for CMOS Image Sensors," ACS Photonics **6**, 1018-1025 (2019).
53. Y. Y. S. E. Sassoon, and T. Treibitz, "Flare in Interference-Based Hyperspectral Cameras," in *Proceedings of the IEEE/CVF International Conference on Computer Vision (ICCV)*(2019), pp. 10174-10182.
54. J. Proust, F. Bedu, B. Gallas, I. Ozerov, and N. Bonod, "All-Dielectric Colored Metasurfaces with Silicon Mie Resonators," ACS Nano **10**, 7761-7767 (2016).
55. P. Hidnert and H. S. Krider, "Thermal Expansion of aluminum and some aluminum alloys," J. Res. Natl. Bur. Stand **48**, 209-220 (1952).
56. V. G. Kravets, A. V. Kabashin, W. L. Barnes, and A. N. Grigorenko, "Plasmonic Surface Lattice Resonances: A Review of Properties and Applications," Chem Rev **118**, 5912-5951 (2018).

57. S. So, T. Badloe, J. Noh, J. Bravo-Abad, and J. Rho, "Deep learning enabled inverse design in nanophotonics," Nanophotonics **9**, 1041-1057 (2020).

58. J. Robinson, and Y. Rahmat-Samii, "Particle Swarm Optimization in Electromagnetics," IEEE Transactions on Antennas and Propagation **52**, 397-407 (2004).

59. A. R. Robertson, "Historical development of CIE recommended color difference equations," Color Res. Appl. **15**, 167-170 (1990).

60. T. Smith, and J. Guild, "The C.I.E. colorimetric standards and their use," Trans. Opt. Soc. **33**, 73-134 (1932).

61. M. R. Luo, G. Cui, and B. Rigg, "The development of the CIE 2000 colour-difference formula: CIEDE2000," Color Res. Appl. **26**, 340-350 (2001).

62. Y. Y, M, Jun, Y, Nenghai, "Color Image Quality Assessment Based on CIEDE2000," Advances in Multimedia **2012**, 1-6 (2012).

63. A. Koschan, and M. Abidi, *Digital Color Image Processing* (John Wiley & Sons, Inc., 2008).

64. M. Erdmanis, and I. Tittonen, "Focused ion beam high resolution grayscale lithography for silicon-based nanostructures," Applied Physics Letters **104** (2014).

65. D. H. Kim, H. J. Lee, H. Jeong, B. Shong, W. H. Kim, and T. J. Park, "Thermal Atomic Layer Deposition of Device-Quality SiO2 Thin Films under 100 degrees C Using an Aminodisilane Precursor," Chem Mater **31**, 5502-5508 (2019).

66. J. S. T. Smalley, X. Ren, J. Y. Lee, W. Ko, W. J. Joo, H. Park, S. Yang, Y. Wang, C. S. Lee, H. Choo, S. Hwang, and X. Zhang, "Subwavelength pixelated CMOS color sensors based on anti-Hermitian metasurface," Nat Commun **11**, 3916 (2020).

67. J. Park, S. Jeon, and S. J. Kim, "Subwavelength, polarimetric color sorting by densely interleaved nano-resonators," Optics Communications

485, 126711 (2021).
68. S. J. Kim, J.-H. Kang, M. Mutlu, J. Park, W. Park, K. E. Goodson, R. Sinclair, S. Fan, P. G. Kik, and M. L. Brongersma, "Anti-Hermitian photodetector facilitating efficient subwavelength photon sorting," Nature Communications **9** (2018).
69. J. Yang, D. Sell, and J. A. Fan, "Freeform Metagratings Based on Complex Light Scattering Dynamics for Extreme, High Efficiency Beam Steering," Annalen der Physik **530** (2018).
70. D. Sell, J. J. Yang, S. Doshay, and J. A. Fan, "Periodic Dielectric Metasurfaces with High-Efficiency, Multiwavelength Functionalities," Adv Opt Mater **5** (2017).
71. S. Jafar-Zanjani, S. Inampudi, and H. Mosallaei, "Adaptive Genetic Algorithm for Optical Metasurfaces Design," Scientific Reports **8** (2018).
72. D. Sell, J. Yang, S. Doshay, R. Yang, and J. A. Fan, "Large-Angle, Multifunctional Metagratings Based on Freeform Multimode Geometries," Nano Letters **17**, 3752-3757 (2017).
73. J. Yang, and J. A. Fan, "Topology-optimized metasurfaces: impact of initial geometric layout," Optics Letters **42**, 3161-3164 (2017).
74. J. K. Guest, J. H. Prevost, and T. Belytschko, "Achieving minimum length scale in topology optimization using nodal design variables and projection functions," Int J Numer Meth Eng **61**, 238-254 (2004).
75. C. Boeddeker, P. Hanebrink, L. Drude, J. Heymann, and R. Haeb-Umbach, "On the Computation of Complex-valued Gradients with Application to Statistically Optimum Beamforming," arXiv pre-print server (2019).
76. S. A. McDonald, G. Konstantatos, S. Zhang, P. W. Cyr, E. J. Klem, L. Levina, and E. H. Sargent, "Solution-processed PbS quantum dot infrared photodetectors and photovoltaics," Nat Mater **4**, 138-142 (2005).
77. P. Martyniuk, and A. Rogalski, "Quantum-dot infrared photodetectors: Status and outlook," Progress in Quantum Electronics **32**,

89-120 (2008).
78. H. Tang, C.-J. Chen, Z. Huang, J. Bright, G. Meng, R.-S. Liu, and N. Wu, "Plasmonic hot electrons for sensing, photodetection, and solar energy applications: A perspective," The Journal of Chemical Physics **152**, 220901 (2020).
79. M. Chen, L. Shao, S. V. Kershaw, H. Yu, J. Wang, A. L. Rogach, and N. Zhao, "Photocurrent enhancement of HgTe quantum dot photodiodes by plasmonic gold nanorod structures," ACS Nano **8**, 8208-8216 (2014).
80. J. Tong, F. Suo, J. Ma, L. Y. M. Tobing, L. Qian, and D. Hua Zhang, "Surface plasmon enhanced infrared photodetection," Opto-Electronic Advances **2**, 18002601-18002610 (2019).
81. N. C. Lindquist, J. Jose, S. Cherukulappurath, X. S. Chen, T. W. Johnson, and S. H. Oh, "Tip-based plasmonics: squeezing light with metallic nanoprobes," Laser & Photonics Reviews **7**, 453-477 (2013).
82. J. A. Schuller, E. S. Barnard, W. Cai, Y. C. Jun, J. S. White, and M. L. Brongersma, "Plasmonics for extreme light concentration and manipulation," Nat Mater **9**, 193-204 (2010).
83. S. Roh, T. Chung, and B. Lee, "Overview of the characteristics of micro- and nano-structured surface plasmon resonance sensors," Sensors (Basel) **11**, 1565-1588 (2011).
84. M. Kauranen, and A. V. Zayats, "Nonlinear plasmonics," Nature Photonics **6**, 737-748 (2012).
85. M. R. Shcherbakov, D. N. Neshev, B. Hopkins, A. S. Shorokhov, I. Staude, E. V. Melik-Gaykazyan, M. Decker, A. A. Ezhov, A. E. Miroshnichenko, I. Brener, A. A. Fedyanin, and Y. S. Kivshar, "Enhanced third-harmonic generation in silicon nanoparticles driven by magnetic response," Nano Lett **14**, 6488-6492 (2014).
86. M. L. Juan, M. Righini, and R. Quidant, "Plasmon nano-optical tweezers," Nature Photonics **5**, 349-356 (2011).
87. X. G. Luo, and T. Ishihara, "Surface plasmon resonant interference

nanolithography technique," Appl Phys Lett **84**, 4780-4782 (2004).
88. K. J. Russell, T. L. Liu, S. Y. Cui, and E. L. Hu, "Large spontaneous emission enhancement in plasmonic nanocavities," Nature Photonics **6**, 459-462 (2012).
89. G. M. Akselrod, C. Argyropoulos, T. B. Hoang, C. Ciraci, C. Fang, J. N. Huang, D. R. Smith, and M. H. Mikkelsen, "Probing the mechanisms of large Purcell enhancement in plasmonic nanoantennas," Nature Photonics **8**, 835-840 (2014).
90. C. Sauvan, J. P. Hugonin, I. S. Maksymov, and P. Lalanne, "Theory of the spontaneous optical emission of nanosize photonic and plasmon resonators," Phys Rev Lett **110**, 237401 (2013).
91. M. I. Stockman, "Nanofocusing of optical energy in tapered plasmonic waveguides," Phys Rev Lett **93**, 137404 (2004).
92. J. Yang, C. Sauvan, A. Jouanin, S. Collin, J. L. Pelouard, and P. Lalanne, "Ultrasmall metal-insulator-metal nanoresonators: impact of slow-wave effects on the quality factor," Optics Express **20**, 16880-16891 (2012).
93. Z. Li, J. L. Kou, M. Kim, J. O. Lee, and H. Choo, "Highly Efficient and Tailorable On-Chip Metal-Insulator-Metal Plasmonic Nanofocusing Cavity," Acs Photonics **1**, 944-953 (2014).
94. C. Zhang, J. M. Fang, W. H. Yang, Q. H. Song, and S. M. Xiao, "Enhancing the Magnetic Resonance via Strong Coupling in Optical Metamaterials," Advanced Optical Materials **5** (2017).
95. S. Dobmann, A. Kriesch, D. Ploss, and U. Peschel, "Near-Field Analysis of Bright and Dark Modes on Plasmonic Metasurfaces Showing Extraordinary Suppressed Transmission," Advanced Optical Materials **2**, 990-999 (2014).
96. H. Choo, M.-K. Kim, M. Staffaroni, T. J. Seok, J. Bokor, S. Cabrini, P. J. Schuck, M. C. Wu, and E. Yablonovitch, "Nanofocusing in a metal–insulator–metal gap plasmon waveguide with a three-dimensional linear taper," Nature Photonics **6**, 838-844 (2012).

97. T. Grosjean, M. Mivelle, F. I. Baida, G. W. Burr, and U. C. Fischer, "Diabolo nanoantenna for enhancing and confining the magnetic optical field," Nano Lett **11**, 1009-1013 (2011).
98. S. J. Kim, S. Yoo, K. Lee, J. Kim, Y. Lee, and B. Lee, "Critical nanofocusing of magnetic dipole moment using a closed plasmonic tip," Optics Express **25**, 14077-14088 (2017).
99. Z. Gao, L. F. Shen, E. P. Li, L. L. Xu, and Z. Y. Wang, "Cross-Diabolo Nanoantenna for Localizing and Enhancing Magnetic Field With Arbitrary Polarization," Journal of Lightwave Technology **30**, 829-833 (2012).
100. N. Zhou, E. C. Kinzel, and X. Xu, "Complementary bowtie aperture for localizing and enhancing optical magnetic field," Opt Lett **36**, 2764-2766 (2011).
101. D. K. Singh, J. S. Ahn, S. Koo, T. Kang, J. Kim, S. Lee, N. Park, and D. S. Kim, "Selective electric and magnetic sensitivity of aperture probes," Opt Express **23**, 20820-20828 (2015).
102. T. Feng, W. Zhang, Z. Liang, Y. Xu, and A. E. Miroshnichenko, "Isotropic Magnetic Purcell Effect," Acs Photonics **5**, 678-683 (2018).
103. J. Zhou, T. Koschny, M. Kafesaki, E. N. Economou, J. B. Pendry, and C. M. Soukoulis, "Saturation of the Magnetic Response of Split-Ring Resonators at Optical Frequencies," Physical Review Letters **95** (2005).
104. B. J. Roxworthy, and K. C. Toussaint, "Simultaneously tuning the electric and magnetic plasmonic response using capped bi-metallic nanoantennas," Nanoscale **6**, 2270-2274 (2014).
105. Y. Chen, Y. H. Chen, J. R. Chu, and X. F. Xu, "Bridged Bowtie Aperture Antenna for Producing an Electromagnetic Hot Spot," Acs Photonics **4**, 567-575 (2017).
106. S. J. Kim, S. E. Mun, Y. Lee, H. Park, J. Hong, and B. x. Lee, "Nanofocusing of Toroidal Dipole for Simultaneously Enhanced Electric and Magnetic Fields Using Plasmonic Waveguide," Journal of Lightwave

Technology **36**, 1882-1889 (2018).

107. I. Fernandez-Corbaton, S. Nanz, and C. Rockstuhl, "On the dynamic toroidal multipoles from localized electric current distributions," Sci Rep **7**, 7527 (2017).

108. D. K. Gramotnev, and S. I. Bozhevolnyi, "Plasmonics beyond the diffraction limit," Nature Photonics **4**, 83-91 (2010).

109. D. K. Gramotnev, D. F. P. Pile, M. W. Vogel, and X. Zhang, "Local electric field enhancement during nanofocusing of plasmons by a tapered gap," Physical Review B **75** (2007).

110. N. A. Issa, and R. Guckenberger, "Optical Nanofocusing on Tapered Metallic Waveguides," Plasmonics **2**, 31-37 (2007).

111. R. Alaee, C. Rockstuhl, and I. Fernandez-Corbaton, "An electromagnetic multipole expansion beyond the long-wavelength approximation," Optics Communications **407**, 17-21 (2018).

초 록

이미지 센서는 환경에 의해 산란되는 전자기파를 전기신호로 바꾸는 소자로, 최근 모바일 기기와 자율 주행 자동차 산업에서 단일 디바이스에 다른 목적을 가진 이미지 센서들이 요구되고 있다. 특히, 디스플레이가 8K 이상의 고해상도로 발전함에 대응하여 1억 화소 이상의 이미지 센서가 개발되고 있다. 그러나, 모바일 기기의 제한된 공간에 의해 고해상도 이미지 센서를 위해서는 센서를 구성하는 픽셀의 크기를 줄여야 하며, 이는 광 효율 감소, 양자 효율 감소, 색 간섭 등의 화질을 감소시키는 요소들을 야기한다.

메타표면은 파장보다 작은 안테나들의 배열을 통해 전자기파를 변조해주는 소자로, 이미지 센서의 광학 시스템을 구성하는 색 필터, 렌즈, 포토 다이오드를 대체하는 소자로 제안되었다. 하지만, 소형화 된 픽셀 크기에 대응하는 메타표면은 나노 안테나의 동작원리와 배열의 한계에 의해 성능이 제한되었다. 본 논문에서는 초소형 픽셀로 구성된 기존 이미지 센서에 대한 화질을 높일 수 있는 메타표면 광학소자를 제시한다.

첫째로, 반사를 억제하는 흡수형 색 필터에 대해서 논의한다. 기존 메타표면 색 필터 소자에서 필연적으로 발생하는 내부 반사는 찍은 이미지에서 플레어 현상을 유발한다. 본 논문에서는 쌍곡 메타물질 안테나의 흡수 공진 대역을 입자 무리 최적화 방식을 이용해 특정 대역 만을 투과하고 나머지는 흡수하는 색 필터를 설계한다. 특히, 255 nm 크기 픽셀의 베이어 패턴 색 필터를 제시한다.

둘째로, 이미지 센서의 광 효율을 높이기 위한 색 분배 메타표

면을 제시한다. 이미지 센서의 포토 다이오드는 밴드 갭 이상의 에너지를 가지는 빛에 대해 전기신호로 변환하므로, 색 구분을 위해 흡수형 색 필터를 사용한다. 이는 하나의 픽셀을 구성하는 청, 녹, 적색 필터에 의해 이미지 센서의 전체 광 효율이 33 %로 제한되는 것을 의미한다. 따라서, 서브 픽셀에 입사하는 빛을 색에 따라 다른 방향으로 빛을 분배하여 기존의 광 효율 한계를 넘어서는 자유형 메타표면 소자를 설계한다.

마지막으로, 저조도의 근적외선에서 신호 대 잡음비를 높일 수 있는 광 집속 소자를 제시한다. 깔대기 모양의 플라즈모닉 개구를 통해 빛을 파장보다 매우 작은 크기의 영역에 집중시킨다. 집속된 전기장과 자기장은 공간적으로 분포된 반도체와 상호작용함으로써, 메타표면의 존재에 따라 강화된 Purcell 효과를 얻는다.

본 박사학위 논문은 이미지 센서를 위한 기존의 제한된 메타표면 소자를 극복하고, 초소형 픽셀의 이미지 센서 개발의 초석이 될 것으로 기대된다. 나아가, 이미지 센서를 구성하는 광학 시스템을 메타표면으로 대체할 새로운 플랫폼을 구축하는 것에 기여할 것으로 기대된다.

주요어: 이미지 센서, 메타표면, 메타표면, 색 필터, 쌍곡 메타물질, 표면 플라즈몬 폴라리톤
학 번: 2015-21010